Revision 1

Weathering of galena: Mineralogical processes, hydrogeochemical fluid path modeling and estimation of the growth rate of pyromorphite

Maximilian F. Keim*, Gregor Markl

Mathematisch-Naturwissenschaftliche Fakultät, Fachbereich Geowissenschaften, Universität Tübingen, Wilhelmstraße 56, D-72074 Tübingen, Germany

* corresponding autor: maximilian-felix.keim@uni-tuebingen.de

Keywords: lead, supergene weathering, phase stabilities, galena, cerussite, anglesite, pyromorphite, reaction path modeling, growth rate

Abstract

In many natural and anthropogenically affected environments, alteration of galena produces thermodynamically more stable secondary lead phases. These secondary minerals control the mobility of the toxic heavy metal lead in water. Their textural, paragenetic and stability relations have not been investigated in detail in the literature yet. An extensive petrographic study of 41 thin sections of weathered, zoned galena and adjacent country rock from the Schwarzwald mining area, southwest Germany is presented. The observed textures were evaluated using PHREEQC fluid path modeling and sequences of stable secondary mineral assemblages were predicted.

The most common secondary (supergene) lead minerals of interest here are cerussite, anglesite and pyromorphite group minerals (PyGM; pyromorphite, mimetite and vanadinite). These lead phases show a spatially well-ordered zoned texture around the preexisting/relic galena. Cerussite and anglesite commonly occur either as in situ replacement of galena and/or as euhedral crystals in cavities of former, partially dissolved galena. The PyGM are present either as crusts around the margin of the former/relic galena or are common as infiltration products into the host rock/gangue. During progressive weathering anglesite typically disappears first followed by cerussite. Finally, only the highly insoluble PyGM persist as a perimorphose. Hence, a spatially and temporally zoning texture is formed.

Thermodynamic models of various fluid evolution paths using PHREEQC show the influence of temperature, pH, variable P_{CO2}, phosphorous contents and/or different mineral reactions on the sequence of formation and stability of the secondary lead phases. Already small changes in one or more of these parameters can lead to different mineral assemblages or sequences of secondary lead minerals. Over almost the whole relevant pH range, PyGM are the most stable lead phases, precipitating at very low ion activities explaining their textural position. Whether cerussite or anglesite forms, depends mainly on the pH value of the supergene fluids, which is

affected by the quite variable fluid pathways. Furthermore a solubility diagram for a typical near-surface fluid was calculated, showing that anglesite is the most soluble phase, followed by cerussite and PyGM. This again reflects the microscopic observations.

As a further step, the time span for the formation of a natural mm-thick pyromorphite crust was evaluated using subsoil phosphorous fluxes from the literature. The calculation indicates that mm-thick pyromorphite crusts can be formed in few tens to about hundred years, which is in agreement with observations in the nature.

In this study, a framework for predicting stable secondary lead mineral assemblages and textures by fluid path modeling is given. These models are potentially important for predicting the retention and mobilization of lead in systems around contaminated sites or natural ore deposits.

Introduction

In lead-bearing ore deposits galena [PbS] is the most common sulfide mineral (e.g., Huff and Lovering 1976; Acero et al. 2007). If galena is exposed to near-surface oxidizing conditions, supergene weathering leads to the formation of thermodynamically more stable secondary lead phases (Park and MacDiarmid 1975; Ruby et al. 1994; Reichert 2007). Depending on the fluid chemistry, anglesite [$PbSO_4$], cerussite [$PbCO_3$], the pyromorphite group minerals (PyGM; pyromorphite [$Pb_5(PO_4)_3Cl$], mimetite [$Pb_5(AsO_4)_3Cl$],vanadinite [$Pb_5(VO_4)_3Cl$]) or other, more rare secondary minerals, are formed (Ruby et al. 1994).

The release of the toxic heavy metal lead into a fluid is controlled by the stability of galena and the secondary lead minerals which are formed during its decomposition (Basta and McGoven 2004). Much is known about galena weathering mechanisms under different chemical conditions (e.g., Zhang and Ryan 1999; Gerson and O`Dea 2003; Mikhlin et al. 2006; Acero et al. 2007; Lara et al. 2011). Experiments from Cama et al. (2005) and De

Giudici et al. (2005) show that dissolution rates are highest at low pH-conditions. Other studies report the enhanced rates of galena dissolution and secondary mineral formation caused by bacterial activity (Bang et al. 1995; Garcia et al. 1995). Anglesite and cerussite are the most abundant alteration products described in oxidation zones worldwide (e.g., Park and MacDiarmid 1975; Szczerba and Sawlowicz 2009; Lara et al. 2011) and often form by direct transformation from galena. The stability relations of cerussite and anglesite are dependent on the pH value, sulfur and lead activity as well as the CO_2-partial-pressure of the near-surface fluid causing the weathering (Ingwersen 1990).

Besides anglesite and cerussite, the above mentioned PyGM are the most important, supergene lead phases (Nriagu 1974; Ingwersen 1990; Niedermayr et al. 1994; Magalhães and Silva 2003). A complete solid solution series is known between pyromorphite and mimetite (Wondratschek 1963; Baker 1966; Markl et al. 2014b), a partial one is known between pyromorphite and vanadinite (Markl et al. 2014b). All PyGM have very low solubilities and are consequently insoluble under most natural environmental conditions (logKs: pyromorphite = -84.4 (Nriagu 1974); mimetite = -76.3 (Bajda 2010); vanadinite = -86.0 (Gerke et al. 2009)). This feature is used to remediate lead contaminated soils by adding phosphate to the contaminated site (e.g., Cotter-Howells et al. 1994; Ruby et al. 1994; Basta and McGoven 2004). Based on oxygen isotopes, Burmann et al. (2013) showed that almost the entire quantity of phosphate fixed in pyromorphite is biologically modified. Because of these biological processes it remains unclear, whether there is an important direct inorganic source of phosphate (like dissolution of apatite). Already published Eh-pH diagrams for the minerals anglesite, cerussite and Cl-pyromorphite are available for fixed lead activities (e.g., Garrels and Christ 1965; Nriagu and Moore 1984). However stability diagrams calculated for variable lead and P activities as well as variable PCO_2 and combining these with fluid path modelling have not yet been published.

The characteristic zoned textures formed during weathering of galena have not been quantitatively evaluated either. They were mentioned by Gerstendörfer (1890) and Niedermayr et al. (1994) for natural samples and by Ruby et al. (1994) for samples in anthropogenic contaminated soils. They observed that galena was converted to cerussite and anglesite and that these fine-grained pseudomorphs were rimmed by pyromorphite or other lead phosphates. These authors and Gonnard (1888) also described the occurrence of empty pyromorphite perimorphoses after galena. In addition Szczerba and Sawlowicz (2009) distinguished different generations of cerussite, namely in situ microcrystalline and later euhedral macrocrystalline forms.

In this paper the first detailed petrographic description of secondary lead mineral zonations is presented. With new stability and solubility diagrams the spatial and temporal stability relations among cerussite, anglesite and PyGM is evaluated. By modeling the weathering of galena fluid evolution paths are established in order to predict the secondary lead mineral assemblages formed in various scenarios of fluid-chemical changes pertinent to oxidation zones in hydrothermal ore deposits or at lead contaminated sites.

Geological background

The sample sites are located in the Schwarzwald (SW-Germany), which is a low mountain range about 50 by 100 km (Fig. 1) and part of the Variscan basement of central Europe (Geyer and Gwinner 2011). The basement is composed of crystalline rocks like gneiss, granite and migmatite (Kalt et al. 2000) and is overlain by Permian and Triassic red-bed sediments and later Triassic and Jurassic terrestrial, fluviatile and marine sediments. The Alpine orogeny induced the opening of a continental rift (Upper Rhinegraben), which resulted in an uplift and an eastward dipping of the eastern rift shoulder along a major fault system (Rhinegraben boundary fault). During the following erosion the basement was partly stripped and widely exposed (Geyer and Gwinner 2011).

The basement as well as the redbed sedimentary cover rocks host more than 1000 hydrothermal veins (Metz et al. 1957), basically containing fluorite, barite, quartz and carbonates as gangue (Bliedtner and Martin 1986). Galena is the most widespread ore mineral in these veins (Metz et al. 1957), occurring unevenly distributed all over the Schwarzwald (Markl et al. 2014b). The supergene weathering of these galena-bearing veins started during the Paleogene (Hautmann and Lippolt 2000), continues until today and produces assemblages of secondary lead minerals described below.

Sample description

In the present study, 41 thin sections of weathered galena and adjacent host rock/gangue from seven different localities were investigated (Table 1, Fig. 1). Macroscopically, one observes an in situ transformation of galena to a mixture of fine-grained cerussite and/or anglesite in small dissolution cavities. PyGM occur at the rim of former or relic galena (Fig. 2A and Fig 2B) or as finely distributed infiltration products in the host rock and gangue. Based on our microscopic observations, the alteration of galena was classified into five different steps (see Fig. 3):

Step 1: Galena is converted in situ to xenomorphic cerussite and anglesite (Fig. 2C) or to cerussite alone. Replacement takes place at the rim of the galena grains as well as along the typical {111} cleavage planes (Fig. 2D). The in situ products are typically interspersed by small galena relics, or more rarely by fine-grained covellite, to an extent that cerussite and anglesite may seem opaque. In our samples, the PyGM do not appear as direct replacement products. However, samples where PyGM directly grow on galena are known (Stack et al. 2004; Ruby et al. 1994). Though, the PyGM in our samples always occur at the rim of weathered galena, separated by a zone of cerussite and/or anglesite. Furthermore, the PyGM appear in the host rock/gangue as fine- to coarse-grained infiltration products (Fig. 2E).

Step 2: During advanced weathering, cavities were formed caused by the dissolution of galena, anglesite and cerussite. The PyGM do not show any dissolution features. Within cavities, euhedral and subhedral anglesite and cerussite crystallize, typically free from galena/covellite remnants (Fig. 2F). In this step, galena is more and more consumed and thicker crusts of PyGM occur along the margins of the weathered galena. Within cavities PyGM often form euhedral, colorful crystals (green, yellow and brown) showing their typical crystal shapes. Furthermore, they occur at the rim as poorly crystalline, spongy, partially colorless masses (Fig. 3G). Growth zonation textures within the PyGM crusts (Fig.3H) or single euhedral crystals are commonly observed.

Step 3: Almost all galena is consumed either converted to anglesite/cerussite or dissolved. Cerussite and anglesite show augmented dissolution textures like skeletal grain boundaries, which are often rounded (Fig. 2I). The infiltration of the host rock/gangue as well as the formation of the PyGM crusts proceeds.

Step 4: Anglesite is completely dissolved, thus only cerussite remains at the position of the former galena (together with partly large cavities), PyGM occur along its former margins. In contrast to the stable PyGM, cerussite typically shows strong dissolution textures.

Step 5: The last step of galena weathering comprises the complete dissolution of cerussite. Consequently, the PyGM crusts remain as empty perimorphoses after galena.

The observations lead to the conclusion that during the advancing weathering of galena the secondary lead minerals form a spatial and temporal zonation. The spatial zonation is galena-cerussite/anglesite-PyGM, the temporal sequence involves initial formation of anglesite and cerussite, then first dissolution of anglesite, later dissolution of cerussite and, finally, only the highly insoluble PyGM remain.

Methods

In order to model fluid evolution paths during the weathering of galena, PHREEQC was used in the version 2.18.3 (Parkhurst and Apello 1999). For calculating stability/predominance diagrams, PHREEPLOT was used in the version 1.0 (Kinnigburgh and Cooper 2011). All calculations are based on the wateq4f.dat database (Ball and Nordstorm 1991).

To receive realistic input parameters for the quantitative hydrogeochemical modeling, various near-surface water samples from the Schwarzwald or similar regions with regards to their pH and their O_2, CO_2, chloride, phosphorous, sulfur and lead concentrations were compared (see Table 2). Based on the average of Mid-European rainwaters (Mrose 1966; Verhoeven et al. 1987; Négrel and Roy 1998; Polkowska et al. 2005) the initial pH of our models was chosen to be 4.9.

Besides oxygen, CO_2 is the most important gaseous phase for mineral-water-reactions (Sigg and Stumm 2011). Due to weathering reactions as well as decomposition of organic matter (Tan 1998), the CO_2 partial pressure of mine water is typically higher than in equilibrium with the atmosphere ($logP_{CO2}$ = -3.55 bar). Water samples of the Schwarzwald have $logP_{CO2}$ between -0.4 and -3.4 bar, with an average of -2.5 bar (Göb et al. 2011, 2013a, 2013b; Markl et al. 2014a). To cover the natural variability, the full range of CO_2 partial pressures was considered in the calculations. The oxygen partial pressure was set to the value of $logP_{O2}$ = -0.68 bar referring to an open system in equilibrium with the atmosphere.

Typical Schwarzwald mine-waters contain chloride concentrations between $3.74x10^{-3}$ M and $5.35x10^{-6}$ M, with an average of $2.60x10^{-4}$ M (Göb et al. 2011, 2013a, 2013b; Markl et al. 2014a). The value of $2.60x10^{-4}$ M was used as average chloride concentration in our models.

Compared to chlorine, phosphorous is much less abundant. Only 35 % of the Schwarzwald mine-water-samples of Göb et al. (2011, 2013a, 2013b) show concentrations above the detection limit with a maximum of $1.22x10^{-6}$ M and an average (excluding the samples below the detection limit) of $3.22x10^{-7}$ M which is consistent with values of Magalhães et al. (1985). Soil water samples from Betzenstein (SE-Germany) show phosphate concentrations up to

$1.29x10^{-5}$ M (Kaiser et al. 2003). In order to reflect the whole range of possible concentrations a range between the maximum observed ($1.29x10^{-5}$ M) and the calculated equilibrium concentration of $3.56x10^{-10}$ M (derived from the congruent dissolution of pyromorphite (logKs from Nriagu 1974)) was chosen.

The sulfur concentration in mine waters ranges from $4.63x10^{-6}$ M to $2.79x10^{-3}$ M, with an average of $1.35x10^{-4}$ M (Göb et al. 2011, 2013a, 2013b; Markl et al. 2014a). Accordingly, an average sulfur concentration of $1.35x10^{-4}$ M for our calculations was chosen.

The lead activity, finally, was treated as variable to reflect the fluctuations expected during discontinuous alteration and dissolution of galena. The temperature was set to 10°C representing the annual average temperature of Lahr (Schwarzwald). The maximum average temperature for Lahr is 20.2°C in the summer (July) and 2.4°C in the winter (January). All phases were treated as pure end members which is very close to microprobe analyses for cerussite and anglesite, close for galena and also close to many PyGM analyses. About 40 % of all analyses are basically pure endmembers (>98 % end member component). Many of these PyGM analyses showed various amounts of Ca substituting for Pb and of arsenate and vanadate substituting for phosphate. However, these modifications do not change the principal validity of our calculations and for many phosphate-dominated systems, they are correct anyway.

Results

Stability relations among anglesite, cerussite and pyromorphite

To evaluate the stability relations among the supergene lead minerals cerussite, anglesite and pyromorphite, stability/predominance diagrams using PHREEPLOT were calculated (Kinnigburgh and Cooper 2011) with regards to variable pH and a_{Pb2+}. Also variable P-contents, Cl-contents and CO_2 partial pressures were included. As PyGM endmember Cl-pyromorphite was used, since it is most common in the investigated samples.

This is how the calculations for the stability diagrams were set up: First, a water was generated with fixed element concentrations of S = $1.35x10^{-4}$ M, Cl = $2.60x10^{-4}$ M, a $logP_{O2}$ of -0.68 bar (fluid 1) and the temperature was fixed to 10°C. As conservative cation, we chose Na^{+} and the charge balance was maintained by adding N(5) (as nitrate). Phosphorous concentration and P_{CO2} were varied stepwise (P in 6, P_{CO2} in 5 steps). The speciation and saturation of this water with respect to the phases of interest was then calculated for pH values from 2 to 10 and for $log(aPb^{2+}/a^2H^{+})$ values from 0 to 10 (see Fig 4A)

At low lead activities, no solid phases are stable, and so the aqueous lead species/complexes Pb^{2+}, $PbCO_3^{0}$ and $Pb(CO_3)_2^{2-}$ contain all Pb in the system. Pb^{2+} is predominant below and the lead carbonate complexes above pH = 7.3 (note: predominance relations of aqueous species only valid for $logP_{CO2}$ = -3.55). With increasing lead activity, Cl-pyromorphite becomes stable over almost the whole pH-range. With lower phosphorous content, the size of the Cl-pyromorphite stability field decreases. The stability of cerussite mostly depends on the $logP_{CO2}$. With increasing partial pressures the stability field is enlarged at the cost of the Cl-pyromorphite and anglesite stability fields. Anglesite is stable at even higher lead activities than cerussite and Cl-pyromorphite. The upper left corner marks the area where lead activity reaches values which are not realized in natural environments. The diagram from Figure 4A is used to plot the following fluid paths.

If phosphorous is fixed and chlorine is varied, OH-pyromorphite is stabilized at very low chlorine contents of approximately $2.60x10^{-7}$ M (see Fig 4B). With even lower chlorine content the Cl-pyromorphite field is getting smaller. OH-dominant pyromorphite is rare in nature (Markl et al. 2014b) as it requires extremely chlorine-poor environments not commonly realized in typical soil water environments. Only closed micro parts of an evolving system may become Cl-depleted and in these "enclaves", OH-pyromorphite may become stable.

253 **Model set up for changes in fluid chemistry during progressive weathering of galena**

254 For a quantitative understanding of the fluid evolution during the supergene weathering of
255 galena, a step-wise weathering model for galena, using PHREEQC was developed (Parkhurst
256 and Apello 1999). The resulting reaction paths were combined with the stability diagram
257 discussed above (Fig. 4A). Calculations involving artificial fluids are shown as steps (1a), (2)
258 and (3) on Fig. 5A, while natural water samples are plotted as steps (1b) and (3) on Fig. 5B.

259 (1a) Generating an artificial fluid before mineral-fluid reaction:

260 A water was generated with a chlorine content of $2.6x10^{-4}$ M, a specific amounts of
261 phosphorous ($1.0x10^{-5}$ M and $1.0x10^{-7}$ M), a specific temperatures (5°C, 10°C and 25°C) and
262 an initial pH value of 4.9. As conservative cation Na^+ was added and the charge balance is
263 maintained using N(5) (as nitrate). Subsequently it was equilibrated with atmospheric P_{O2}
264 before and during any further reaction, simulating an open system with regards to the
265 atmosphere. It is assumed that the supergene minerals usually do not form under low-P_{O2}
266 conditions, because mine waters of Bucher et al. (2009) show no significant changes in their
267 P_{O2}. This water was then equilibrated during any further reaction step with different CO_2
268 partial pressures (log P_{CO2} = -0.4 bar,-2,5 bar and -3.4bar) simulating an open soil system,
269 which generates different P_{CO2} due to organic decomposition reactions.

270 (1b) Natural water samples as input:

271 Also natural water samples from the Schwarzwald mining district with their specific ion
272 concentration as initial fluids were used (Göb et al. 2011, 2013a, 2013b; Markl et al. 2014a).
273 Charge balance for these waters was forced using HCO_3^-.

274 (2) Reaction with the host rock/gangue:

275 Based on microscopic observation of the host rock mineralogy, the natural artificial (1b)
276 water samples were equilibrated with quartz, kaolinite (representing the clay mineral
277 component in the host rocks), muscovite, annite (representing the host-rock biotite) and

goethite as a proxy of altered/weathered gneiss at the Feldberg and Lisbühl localities. One model also includes a reaction with the sulfide pyrite, another one with siderite and a further one with anorthite, as all these phases are pertinent to one or the other locality.

(3) Reaction with galena:

The calculated water with specific pH value and element content (1a) as well as the natural water samples (1b) were now reacted incrementally with galena in 250 individual steps. In every single step 9.6×10^{-7} mol galena were added to the fluid phase. This corresponds to a total amount of 2×10^{-4} mol galena. In each reaction step the minerals anglesite, cerussite and Cl-pyromorphite were allowed to precipitate from the solution, if supersaturated (saturation index > 0.0). These assumption neglects, that solids can be supersaturated in the fluid phase without precipitation because of kinetic reasons (see natural water samples, below). After precipitating the solids, their components were subtracted from further reaction steps. All precipitating phases were treated as pure end-members (see above).

Discussion

Quantitative fluid evolution path models for the Feldberg locality

Influence of different P_{CO2} and P-contents: Three different fluid evolution paths with high P_{CO2} and high P-content ((a) red path), low P_{CO2} and high P-content ((b) purple path) and with low P_{CO2} and low P-content ((c) brown path) were modeled and visualized in Fig. 6A. These paths are used to simulate changing conditions in the soil. For example, the amount of phosphorous and carbon leached are dependent on seasonal variations (e.g., Kaiser et al. 2003).

(a) Due to its high P_{CO2} the water has a low pH value of approximately 4.9, which is similar to the initial one. With increasing amounts of galena reacting, the lead activity rises and the water reaches the Cl-pyromorphite stability field at which the pH value shows no

303 significant change. If the fluid path hits the boundary between cerussite and Cl-
304 pyromorphite, both minerals precipitate. The amount of galena reacting does not suffice to
305 reach the anglesite stability field.

306 (b) The water has a pH value of around 6.4 and also reaches firstly the Cl-pyromorphite
307 stability field. Subsequently, the fluid path evolves towards lower pH values. The extent
308 of this pH-decrease depends on the concentration as well as on the
309 speciation/complexation of the involved ions. A proton-generating reaction is favored in
310 acid (see Eq. (1)), a proton-consuming reaction in more basic environments. The log(Ks)
311 of the reaction was calculated for 25 °C and 1 bar using the SUPCRT92 software
312 (Johnson et al. 1992) augmenting the SUPCRT92 database DPRON92 with pyromorphite
313 thermodynamic data from Bisengalieva et al. (2010).

314 $5Pb^{2+}+3H_2PO_4^-+Cl^- = Pb_5(PO_4)_3Cl+6H^+$ (1) log (Ks) = 21.00

315 The fluid path subsequently reaches the boundary between Cl-pyromorphite and anglesite
316 at which both minerals precipitate. At last the path ends in the anglesite stability field.

317 (c) The water has the same initial pH value as fluid path (2). Because of its lower P-
318 content it reaches the Cl-pyromorphite stability field at higher lead activities. The small
319 amount of Cl-pyromorphite precipitating leads to no significant pH change. Before
320 reaching the cerussite stability field, the fluid path evolves to slightly lower pH values.
321 This is probably the result of water hydrolysis in the presence of Pb^{2+} ions. The path
322 reaches the triple point between Cl-pyromorphite, cerussite and anglesite and lastly ends
323 up precipitating anglesite and cerussite.

324 The modeled paths are in good agreement with the observations of galena alteration at the
325 Feldberg locality. The textural position of pyromorphite at the rim or in the adjacent host
326 rock/gangue is explained by its precipitation at low lead activities. The paths also explain
327 why in situ transformation of galena to cerussite and anglesite in textural coexistence is a

common observation (see Fig. 3C). Interestingly, whether a fluid precipitates anglesite or cerussite or both can be influenced by the P_{CO2} and the P-content of the supergene water. P-content and P_{CO2} are both dependent on seasonal fluctuations (see Kaiser et al. 2003).

Influence of temperature: Three different fluid evolution paths with different temperatures of T = 25°C ((d) red path), T = 10°C ((e) purple path) and T = 5°C ((f) brown path) were modeled and visualized in Fig. 6B to show the influence of variable ambient temperature again due to seasonal variations. The $\log P_{CO2}$ was fixed to -2.5, the P-concentration to $1x10^{-5}$ M. While the speciation and thereby the fluid evolution paths change, the size of the stability fields does not.

(d) After equilibration with the altered gneiss, the water has a pH value of 5.8. With increasing lead activity, the water reaches first the Cl-pyromorphite and then the anglesite stability field.

(e, f) The waters have an initial pH value of 5.98 (b) and of 5.87 (c), respectively. Both paths also reach firstly the Cl-pyromorphite stability field. Subsequently, they additionally reach the cerussite stability field. At the end of the paths anglesite and cerussite coprecipitate.

The models including different temperatures show that minor changes in the physical property of water reacting with galena can influence the formation of secondary lead minerals. Although water with lower temperatures dissolves more CO_2, the fluid path shows the highest pH. The reason for this apparent discrepancy is the temperature-dependent formation of aluminum hydroxy-complexes (more hydroxy-complexes at higher temperatures), which lower the pH value at higher temperatures.

Influence of anorthite and siderite: At the Feldberg locality, former plagioclase is typically intensely altered to clay minerals. In addition, goethite pseudomorphs testify to the former presence of siderite. In order to model the influence of former anorthite (representing plagioclase), First a model water was equilibrated with anorthite ((g) red path) and second reacted two waters with anorthite of $1x10^{-4}$ M ((h) purple path) and $1x10^{-5}$ M ((i) brown path) (Fig. 6C). Due to the resulting calcite supersaturation, calcite is allowed to precipitate from the fluids. If the solution is held supersaturated with regards to calcite, a pH above 10 will result. This pH-value is unrealistically high for the Schwarzwald because the mine, surface and well water analyses from Göb et al. (2011, 2013a, 2013b) and Markl et al. (2014a) vary only between 4.6 and 8.6. In addition, two waters were equilibrated with siderite ((j) yellow path, (k) blue path). Because of supersaturation with respect to $Fe(OH)_3$, goethite was allowed to precipitate in the fluid paths (k).

(g, h, i) The waters have quite different pH-values after reaction with anorthite, ranging from 6.0 (i) over 6.7 (h) to 7.6 (g). All fluid paths reach the Cl-pyromorphite stability field first. Afterwards all paths hit the boundary between Cl-pyromorphite and cerussite. Unlike path (g), paths (h) and (i) finally reach the anglesite stability field.

(j, k) After reacting with siderite the two waters have different pH values of 8.1 (j) and 6.0 (k). Both fluid paths reach the Cl-pyromorphite stability field first, and then the boundary between Cl-pyromorphite and cerussite. Only if $Fe(OH)_3$ is precipitated the fluid path reaches the anglesite stability field (k).

The secondary mineral formation depends on the relative amount of anorthite reacting with the water. At low water/rock ratios, it is highly probable to form only cerussite and Cl-pyromorphite (g). At higher water/rock ratios (h, i) anglesite precipitates in addition at higher lead activities. The influence of siderite on the secondary mineral formation is

dependent on the precipitation of $Fe(OH)_3$. If $Fe(OH)_3$ does not precipitate, pH-values of approximately 8.1 are maintained and only cerussite and Cl-pyromorphite are stable. If $Fe(OH)_3$ precipitates, the pH adjusts to lower values and anglesite forms as well.

Quantitative fluid evolution path models for the Lisbühl locality

Influence of pyrite: For the Lisbühl locality, four different fluid evolution paths with various amounts of pyrite were calculated, showing the influence of additional sulfides on the stability relations/sequences (Fig. 7A): $1x10^{-4}$ mol ((l) red path), $5x10^{-5}$ mol ((m) purple path), $1x10^{-5}$ mol ((n) brown path) and $5x10^{-6}$ mol ((o) yellow path).

(l, m, n) Dependent on the amount of pyrite reacting, the water has pH values of 3.9 (l), 4.3 (m) and 5.6 (n). This decrease of pH value is caused by the release of protons during inorganic oxidation of pyrite (Eq. (2)). Note that also bacterially mediated oxidation of metal sulfides like pyrite will cause an acidification of the fluids (e.g., Donati and Sand 2007).

$$FeS_2+H_2O+7/2O_2 = Fe^{2+}+2SO_4^{2-}+2H^+ \qquad (2)$$

The paths reach at first the Cl-pyromorphite stability field. With increasing lead activity, they all end up in the anglesite stability field.

(o) The water sample with the lowest amount of pyrite reacting has the highest pH value of 5.8 and reaches again firstly the Cl-pyromorphite stability field. The path then reaches the cerussite stability field and finally ends up coprecipitating anglesite and cerussite.

At the Lisbühl locality, slightly altered pyrite grains are typically rimmed by anglesite (see Fig. 8). These samples are by far the ones with the highest amount of anglesite. This observation can be explained by the model results, namely that pyrite grains generate low-pH microenvironments during weathering (paths (l), (m), (n)) which stabilize anglesite. Only if the amount of pyrite reacting is low (path (o)) cerussite forms in addition.

402

403 **Fluid evolution of natural water samples**

404 With the help of natural water samples, the possible secondary lead mineral assemblages
405 precipitating from these specific fluids were predicted. For this purpose, water samples from
406 Göb et al. (2011, 2013a, 2013b) and Markl et al. (2014a) were chosen. None of these water
407 samples are supersaturated with regards to cerussite or anglesite but four water samples are
408 supersaturated with respect to Cl-pyromorphite. For modeling, seven different mine water
409 analyses were selected (maximum and minimum pH and P_{CO2} as well as different amounts of
410 P and Pb (see Fig. 7B). All considered water analyses come from localities where primary
411 and/or secondary lead phases occur.
412 The water samples with the lowest pH value of 4.6 ((1) Segen Gottes) and 5.5 ((2)
413 Silbergründle) are both free of phosphorous and have low $\log P_{CO2}$ of -1.1 and -1.7,
414 respectively. Both fluid paths end up in the anglesite stability field. Due to its higher lead
415 activity, the sample from Segen Gottes (1) reaches the anglesite stability field earlier.
416 The waters containing phosphorous have intermediate pH values of 6.83 ((3) Kammendobel),
417 7.40 ((4) Straßburgerstollen), 7.60 ((5) Schauinsland) and 7.71 ((6) Wittichen). The samples
418 (5) and (3) are supersaturated with respect to Cl-pyromorphite. In order to reach the Cl-
419 pyromorphite stability field, the samples (4) and (6) need higher lead activities. All fluid paths
420 subsequently reach the cerussite stability field at specific P_{CO2} and end up precipitating
421 cerussite as well as anglesite.
422 The sample with the highest pH-value of 8.6 ((7) Otto) is free of phosphorous and has the
423 lowest $\log P_{CO2}$ of -3.2. The sample only precipitates cerussite and does not reach the anglesite
424 stability field. All these results agree well with observations in nature at the specific localities.
425 For example, anglesite is the main secondary mineral replacing galena at the Segen Gottes
426 locality. In contrast to that, cerussite is the main secondary mineral at the Otto mine.

427

Solubility Diagram

For evaluating the solubility of the minerals cerussite, anglesite and Cl-pyromorphite, a solubility diagram using PHREEQC was calculated (Parkhurst and Apello 1999) (Fig. 9A). The minerals were equilibrated with fluid 1 (see above). Cl-pyromorphite is by far the most insoluble mineral phase under almost all natural conditions. Only below pH = 3.0 anglesite is less soluble than Cl-pyromorphite. Cerussite is less soluble than anglesite over the pH-range of pH = 4.3 to pH = 9.8. Under most pH conditions relevant to nature the increasing solubility of the minerals is: Cl-pyromorphite < cerussite < anglesite. This explains the observed temporal sequence of the secondary lead phases described above.

Pyromorphite growth rate estimation

Formation rates of phosphate minerals at Earth surface conditions are difficult to predict. Laboratory experiments show fast precipitation of phosphates from aqueous solutions within minutes (Ruby et al. 1994 and references therein). Hence, we try to estimate the growth rates of pyromorphite using natural phosphorous fluxes from the subsoil measured over the time period of 2 ½ years by Kaiser et al. (2003).

For the calculation several assumptions were made. Firstly, phosphorous must be the limiting element for pyromorphite formation. This is reasonable because in oxidation zones of Pb-bearing deposits, lead and chloride ions are abundant. Secondly, it is assumed that almost 100 % of the phosphorous from the fluid will be fixed by pyromorphite. This assumption is supported by the very low solubility product of pyromorphite (logKs = -84.5 from Nriagu 1974). Thirdly, the temporal flux of phosphorous must be known (see Kaiser et al. 2003). Fourth, Kaiser et al. (2003) measured the total phosphorous flux as dissolved organic phosphorous and inorganic orthophosphate, pyrophosphate and condensed phosphates. Organic phosphorous is by far the dominant P form in these soil/subsoil systems. For the model it is assumed that all organic P compounds are incorporated during pyromorphite

454 precipitation. Note that all P fixed in pyromorphite is considered to be derived from the soil as
455 it seems to be modified by biological activity (see Burmann et al. 2013). The phosphorous
456 flux varies with the seasons higher fluxes in the summer and autumn contrast with lower
457 fluxes in the spring and winter. Higher fluxes are generated by increasing water amount and
458 higher microbiological activity. Almost all of the organic P is in the mobile hydrophilic
459 fraction and therefore it is assumed that it will be transported easily to groundwater systems
460 (Kaiser et al. 2003).
461 Because all these assumptions are reasonably met, it should be possible to calculate the
462 growth rate of pyromorphite with great confidence.
463 The amount of phosphorous present in a certain volume of pyromorphite is n_{Pyr} (Eq. (3)) and
464 is dependent on the volume of the crust (V_{crust}), the density (ρ_{Pyr}) (a massive crust without
465 porosity is assumed) and molar mass (M_{Pyr}) of pyromorphite. V_{crust} is dependent on the crust
466 thickness (z), growing on a hypothetical 1cm³ galena cube (Eq. (4)).

$$n_{Pyr} = \frac{3 \times V_{crust} \times p_{Pyr}}{M_{Pyr}} \quad (3)$$

$$V_{crust} = (1 + 2z)^3 - 1 \quad (4)$$

467 The amount of phosphorous leached over a certain time period and a certain area (A) from the
468 subsoil is the total phosphorous flux (P_{flux}) (Eq. (5)). Kaiser et al. (2003) determined a
469 phosphorous flux F (in mol/m²/year) over one year and a drainage area of one square meter.

$$P_{flux} = \frac{F}{M_{Pyr} \times 1000} \quad (5)$$

470 The quotient of n_{Pyr} and P_{flux} shows the dependence between growth rate and dewatered area.
471 By the expansion of the term (1/A) it is possible to determine the growth rate in dependence
472 of the thickness of the growing pyromorphite crust (z; expressed as V_{crust}) and the dewatered
473 area (A). This leads to equation (6) illustrated in Figure 10.

$$growth\ duration = \left(\frac{3 \times V_{crust} \times \rho_{pyr}/M_{Pyr}}{F/(M_P \times 1000)}\right) \times \frac{1}{A} \quad (6)$$

With this equation it is possible to estimate, how long it takes to form a crust of one millimeter thickness around a 1 cm³ galena cube. Dewatering 1 m² subsoil with a phosphorous flux of 38.6 mg/m²/year (Kaiser et al. 2003; year 1998/1999), applying a density of pyromorphite of 7.1 g/cm³ (Shackelford and Doremus 2008) leads to a growth duration of about 9 years. It is also possible to plot the growth duration versus the thickness of the growing crust (Fig. 11A). For this calculation, the dewatered area was fixed to 1 m². Furthermore, the dependence of dewatered area and duration of growth, by fixing the thickness of the crust was calculated (Fig 11B).

The calculations seem to be in good agreement with natural observations of a few mm-thick pyromorphite crusts growing as sinters at the pit walls of old mines (Fig. 11C). The calculations show that such crusts can form within time periods of a few years to some hundreds of years, depending on the leached area and the amount of phosphorous available.

Implications

The knowledge on secondary mineral stability relations is important to evaluate the mobilization of elements like lead, which are known for their toxicity. Often it remains unclear which secondary mineral is formed under near-surface conditions. The stability of the secondary mineral is crucially dependent on the participating fluid, which interacts with the primary ore as well as the host rock/gangue. This contribution presents hydrogeochemical models of Pb dissolution and reprecipitation during weathering of ore deposits containing galena. These models offer also a tool to predict retention and/or mobilization of lead which may be applicable to remediation of lead-contaminated sites or during heap leaching. The purely thermodynamic models (i.e., neglecting kinetics) reproduce the observed secondary

497 mineral associations formed during low temperature processes very well and thus prove the
498 applicability of these models to weathering phenomena of ore deposits.
499

500 **Acknowledgments**

501 We are grateful to Udo Neumann for his friendly assistance identifying minerals by ore
502 microscopy, Indra Gill-Kopp for the professional preparation of the samples, Kai Hettmann
503 for his helping hand at the beginning of the hydrogeochemical modeling, Susanne Göb for her
504 help with the water data and finally Stefan Kreissl for the numerous discussions.
505

References cited

Acero, P., Cama, J., and Ayora, C. (2007) Rate law for galena dissolution in acidic environment. Chemical Geology, 245, 219-229.

Bajda, T. (2010) Solubility of mimetite Pb5(AsO4)3Cl at 5-55°C. Environmental Chemistry, 7, 268-278.

Baker, W.E. (1966) An X-ray diffraction study of synthetic members of the Pyromorphite Series. American Mineralogist 51, 1712-1721.

Ball, J.W., and Nordstrom, D.K. (1991) User's manual for WATEQ4F, with revised thermodynamic data base and test cases for calculating speciation of major, trace, and redox elements in natural waters. U.S. Geological Survey Open-File Report, 91-183.

Bang, S.S., Deshpande, S.S., and Han, K.N. (1995) The oxidation of galena using *Thiobacillus ferrooxidans* and *Thiobacillus thiooxidans*. Hydrometallurgy, 37(2), 181-192.

Basta, N.T., and McGowen, S.L. (2004) Evaluation of chemical immobilization treatments for reducing heavy metal transport in a smelter-contaminated soil. Environmental pollution, 127(1), 73-82.

Bisengalieva, M.R., Ogorodova, L.P., Vigasina, M.F., and Mel'chakova, L.V. (2010) Calorimetric determination enthalpy of the formation of natural pyromorphite. Russian Journal of Physical Chemistry A, 84(11), 1838-1840.

Bliedtner, M., and Martin, M. (1986) Erz- und Minerallagerstätten des mittleren Schwarzwaldes, 782 p. LGRB, Freiburg.

Bucher, K., Zhu, Y., and Stober, I. (2009) Groundwater in fractured crystalline rocks, the Clara mine, Black Forest (Germany). International Journal of Earth Sciences, 98(7), 1727-1739.

Burmann, F., Keim, M.F., Oelmann, Y., Teiber, H., Marks, M.A., and Markl, G. (2013) The source of phosphate in the oxidation zone of ore deposits: Evidence from oxygen isotope compositions of pyromorphite. Geochimica et Cosmochimica Acta, 123, 427-439.

Cama, J., Acero, P., Ayora, C., and Lobo, A. (2005) Galena surface reactivity at acidic pH and 25°C based on flow-through and in situ AFM experiments. Chemical geology, 214(3), 309-330.

Cotter-Howells, J.D., Champness, P.E., Charnocky, J., and Pattrick, R.A.D. (1994) Identification of pyromorphite in mine-waste contaminated soils by ATEM and EXAFS. European Journal of Soil Science, 45(4), 393-402.

De Giudici, G., Rossi, A., Fanfani, L., and Lattanzi, P. (2005) Mechanisms of galena dissolution in oxygen-saturated solutions: Evaluation of pH effect on apparent activation energies and mineral-water interface. Geochimica et Cosmochimica Acta, 69(9), 2321-2331.

Donati, E.R., and Sand, W. (2007) Microbial processing of metal sulfides, 314 p. Springer, Dordrecht.

Garcia, O. Jr, Tuovinen, O.H., and Bigham, J.M. (1995) Oxidation of galena by *Thiobacillus ferrooxidans* and *Thiobacillus thiooxidans*. Canadian Journal of Microbiology, 41(6), 508-514.

Garrels, R.M., and Christ C.L. (1965) Solutions, minerals, and equilibria, 450 p. Harper and Row, New York.

Gerke, T.L., Scheckel, K.G., and Schock, M.R. (2009) Identification and distribution of vanadinite (Pb5 (V5+ O4) 3Cl) in lead pipe corrosion by-products. Environmental Science & Technology, 43(12), 4412-4418.

Gerson, A.R., and O'Dea, A.R. (2003) A quantum chemical investigation of the oxidation and dissolution mechanisms of Galena. Geochimica et Cosmochimica Acta, 67(5), 813-822.

Gerstendörfer, J. (1890) Die Mineralien von Mies in Böhmen. Sitzungsberichte der kaiserlichen Akademie der Wissenschaften, Mathematisch-Naturwissenschaftliche Classe, 99, 422-465. (in German)

Geyer, O.F., and Gwinner, M.P. (2011) Geologie von Baden Württemberg, 627 p. Schweizerbart'sche Verlagsbuchhandlung, Stuttgart. (in German)

Göb, S., Gühring, J.E., Bau, M., and Markl, G. (2013a) Remobilization of U and REE and the formation of secondary minerals in oxidized U deposits. American Mineralogist, 98(4), 530-548.

Göb, S., Loges, A., Nolde, N., Bau, M., Jacob, D.E., and Markl, G. (2013b) Major and trace element compositions (including REE) of mineral, thermal, mine and surface waters in SW Germany and implications for water–rock interaction. Applied Geochemistry, 33, 127-152.

Göb, S., Wenzel, T., Bau, M., Jacob, D.E., Loges, A., and Markl, G. (2011) The redistribution of rare-earth elements in secondary minerals of hydrothermal veins, Schwarzwald, southwestern Germany. Canadian Mineralogist, 49(5), 1305-1333.

Gonnard, F. (1888) Pseudomorphs in the Lead Mines of the Puy de Dome. Comptes Rendus Chimie, 105, 1267-1269.

Hautmann, S., and Lippolt, H.J. (2000) 40Ar/39Ar dating of central European K-Mn oxides-a chronological framework of supergene alteration processes during the Neogene. Chemical Geology, 170(1), 37-80.

Huff, L.C., and Lovering, T. (1976) Migration of lead during oxidation and weathering of lead deposits. Geological Survey Professional Paper 957, 21-24.

Ingwersen, G. (1990) Die sekundären Mineralbildungen der Pb-Zn-Cu-Lagerstätte Tsumeb, Namibia (Physikalisch-chemische Modelle), 233 p. Ph.D. thesis, University Stuttgart, Stuttgart. (in German)

Johnson, J.W., Oelkers, E.H., and Helgeson, H.C. (1992) SUPCRT92: A software package for calculating the standard molal thermodynamic properties of minerals, gases, aqueous species, and reactions from 1 to 5000 bar and 0 to 1000 °C. Computers & Geosciences, 18(7), 899-947.

Kaiser, K., Guggenberger, G., and Haumaier, L. (2003) Organic phosphorus in soil water under a European beech (*Fagus sylvatica L.*) stand in northeastern Bavaria, Germany: seasonal variability and changes with soil depth. Biogeochemistry, 66(3), 287-310.

Kalt, A., Altherr, R., and Hanel, M. (2000) The Variscan basement of the Schwarzwald. Supplement to European Journal of Mineralogy. 12, 1-43.

Kinniburgh, D., and Cooper, D. (2011) PhreePlot Creating graphical output with Phreeqc. User Manual. 586 p. (available at: http://www.phreeplot.org/)

Lara, R.H., Briones, R., Monroy, M.G., Mullet, M., Humbert, B., Dossot, M., Naja, G.M., and Cruz, R. (2011) Galena weathering under simulated calcareous conditions. Science of the total Environment, 409, 3971-3979.

Magalhães, M.C.F., Jesus, J.D.P., and Williams, P.A. (1985) The chemistry of uranium dispersion in groundwaters at the Pinhal do Souto mine, Portugal. Inorganica Chimica Acta, 109(2), 71-78.

Magalhães, M.C.F., and Silva, M.C.M. (2003) Stability of lead (II) arsenates. Monatshefte für Chemie , 134(5), 735-743.

Markl, G., Marks, M.A., and Derrey, I. (2014a) Weathering of cobalt arsenides: Natural assemblages and calculated stability relations among secondary Ca-Mg-Co arsenates and carbonates. American Mineralogist, 99(1), 44-56.

Markl, G., Marks, M.A., Holzäpfel, J., and Wenzel, T. (2014b) Major, minor, and trace element composition of pyromorphite-group minerals as recorder of supergene weathering processes from the Schwarzwald mining district, SW Germany. American Mineralogist, 99(5-6), 1133-1146.

Metz, R., Richter, M., and Schürenberg, H. (1957) Die Blei-Zink-Erzgänge des Schwarzwaldes, 277 p. Beihefte zum Geologischen Jahrbuch, 29. (in German)

Mikhlin, Y.L., Romanchenko, A.S., and Shagaev, A.A. (2006) Scanning probe microscopy studies of PbS surfaces oxidized in air and etched in aqueous acid solutions. Applied Surface Science, 252(16), 5645-5658.

Mrose, H. (1966) Measurements of pH, and chemical analyses of rain-, snow-, fog-water. Tellus, 18(2-3), 266-270.

Négrel, P., and Roy, S. (1998) Chemistry of rainwater in the Massif Central (France): a strontium isotope and major element study. Applied Geochemistry, 13(8), 941-952.

Niedermayr, G., Bojar, H.P., Brandstätter, F., Hammer, V.M.F., Moser, B., Postl, W., and Taucher, J. (1994) Neue Mineralfunde aus Österreich XIIIL, 243-275. (in German)

Nriagu, J.O. (1974) Lead orthophosphates - IV Formation and stability in the environment. Geochimica et Cosmochimica Acta, 38(6), 887-898.

Nriagu, J.O., and Moore, P.B. (1984) Phosphate Minerals, 442 p. Springer, Heidelberg.

Park, C.F., and MacDiarmid, R.A. (1975) Ore Deposits, 985 p. W.H. Freeman and Company, San Francisco.

Parkhurst, D.L., and Appelo, C.A.J. (1999) User's guide to PHREEQC (ver. 2)-A computer program for speciation, batch-reaction, one-dimensional transport, and inverse geochemical calculations. U.S. Geological Survey Water-Resources Investigations Report, 99-4259.

Polkowska, Ż., Astel, A., Walna, B., Małek, S., Mędrzycka, K., Górecki, T., and Namieśnik, J. (2005) Chemometric analysis of rainwater and throughfall at several sites in Poland. Atmospheric Environment, 39(5), 837-855.

Reichert, J. (2007) A metallogenetic model forcarbonate-hosted non-sulphide zinc depositsbased on observations of Mehdi Abad and Irankuh,Central and Southwestern Iran, 152 p. Ph.D. thesis, Martin-Luther-University, Halle-Wittenberg.

Ruby, M.V., Davis, A., and Nicholson, A. (1994) In situ formation of lead phosphates in soils as a method to immobilize lead. Environmental Science & Technology, 28(4), 646-654.

Shackelford, J.F., and Doremus, R.H. (2008) Ceramic and Glass Materials: Structure, Properties and Processing, 201 p. Springer Science+Business Media, New York.

Sigg, L., and Stumm, W. (2011) Aquatische Chemie - Einführung in die Chemie natürlicher Wässer, 522 p. vdf Hochschulverlag AG ETH Zürich UTB, Zürich. (in German)

Stack, A.G., Erni, R., Browning, N.D., and Casey, W.H. (2004) Pyromorphite growth on lead-sulfide surfaces. Environmental Science & Technology, 38(21), 5529-5534.

Szczerba, M., and Sawlowicz, Z. (2009) Remarks on the origin of cerussite in the Upper Silesian Zn-Pb deposits, Poland. Mineralogia, 40 (1-4), 54-64.

Tan, K.H. (1998) Principles of Soil Chemistry, 521 p. Marcel Dekker Inc., New York.

Verhoeven, W., Herrmann, R., Eiden, R., and Klemm, O. (1987) A comparison of the chemical composition of fog and rainwater collected in the Fichtelgebirge, Federal Republic of Germany, and from the South Island of New Zealand. Theoretical and applied climatology, 38(4), 210-221. (in German)

Wondratschek, H. (1963) Untersuchngen zur Kristallchemie der Blei-Apatite (Pyromorphite). Neues Jahrbuch für Mineralogie Abhandlungen, 99, 113–160. (in German)

Zhang, P., and Ryan, J.A. (1999) Formation of chloropyromorphite from galena (PbS) in the presence of hydroxyapatite. Environmental Science & Technology, 33(4), 618-624.

657 **Figure captions**

658

659 **Figure 1.** Simplified geological map with the major units and main tectonics of the
660 Schwarzwald (modified after Kalt et al. 2000). The sample locality numbers 1-7 refer to Table
661 1. Abbreviations: BBZ = Baden-Baden Zone; BLZ = Badenweiler Lenzkirch Zone; NSGG,
662 CSGC and SSGC = Northern-, Central- and Southern Gneiss Complex.

663

664 **Figure 2.** (**A**) Photograph of relic galena, which is in situ converted to a mixture of cerussite
665 and anglesite. Additional small dissolution cavities occur. PyGM as brown-yellow-green-crust
666 at the rim. Width of photograph (WoP) is about 3 cm. (**B**) Photograph of former galena, which
667 is completely converted to whitish cerussite and anglesite. PyGM occur at the rim and within
668 cavities. WoP is about 3.5 cm. (**C**) Reflected light image of galena (white) with typical
669 polishing scratches, which is in situ converted to cerussite (light grey) and anglesite (dark
670 grey). WoP is about 430 µm. (**D**) Reflected light image of galena (white) with characteristic
671 triangular pits. Galena is in situ converted to cerussite (light grey) along the {111} cleavage
672 planes. WoP is about 430 µm. (**E**) Reflected light image with crossed polarizers of PyGM
673 infiltratred, altered gneiss consisting of muscovite, clay minerals and quartz. WoP is about
674 860 µm. (**F**) Reflected light image of euhedral anglesite crystals. WoP is about 430 µm. (**G**)
675 Reflected light image with crossed polarizers showing a zonation with cerussite and anglesite
676 (right side; light gray and dark grey) overgrown by a crust of pyromorphite (middle; white
677 and green) as well as vanadinite (left side; brown). WoP is about 3.5 mm. (**H**) Reflected light
678 image with crossed polarizers of well zoned, fine grained whitish pyromorphite overgrown by
679 vanadinite (brown). WoP is about 860 µm. (**I**) Reflected light image of skeletal cerussite
680 crystals. WoP is about 860 µm. Abbreviations: Pyr = pyromorphite Van = vanadinite, Ang =
681 anglesite; Cer = cerussite; Gn = galena; Ms = muscovite; Qz = quartz; Cm = clay minerals.

682

683 **Figure 3.** Sketches showing the different galena weathering steps 1-5 (explanation in the
684 text). Abbreviations: PyGM= pyromorphite group minerals, Ang = anglesite; Cer = cerussite;
685 Cv = covellite; Gn = galena; cryst = crystal.
686
687 **Figure 4.** log(aPb/a^2H^+)-pH-diagrams showing the stability relations of the most important
688 secondary lead minerals as well as the predominance relations between some lead
689 ions/complexes. Diagram (A) shows stability relation at variable P_{CO2} and P-contents (B) is
690 calculated with variable Cl contents. Notice, the continuous lines are only valid for the values
691 illustrated in the lower right corner. *Maximum P-concentration (Kaiser et al. 2003);
692 **Equilibrium concentration of P derived from pyromorphite solubility product (LogKs from
693 Nriagu (1974)).
694
695 **Figure 5.** Flow chart, illustrating the model approach for (**A**) the artificial water samples and
696 (**B**) the natural water samples using PHREEQC. Abbreviations: EQ = equilibration; Si =
697 saturation index; T = temperature; Ang = anglesite; Cer = cerussite; Cl-Pyr = Cl-
698 pyromorphite; Ant= annite; Goe = goethite; Kao = kaolinite; Ms= muscovite and Qz = quartz.
699
700 **Figure 6.** log(aPb/a^2H^+)-pH-diagrams owing the stability relations of the most important
701 secondary lead minerals as well as the predominance relations between some lead
702 ions/complexes. In the diagram 6A different fluid evolution paths in relation to variable P_{CO2}
703 and P-content (including fluid paths (a), (b), (c)), in 6B different temperatures (including fluid
704 paths (d), (e), (f)), and in 6C different amounts siderite and anorthite reacting with the water
705 (including fluid paths (g), (h), (i), (j), (k)) are plotted. Notice, the continuous lines are only
706 valid for the values illustrated in the lower right corner. *Maximum P-concentration (Kaiser
707 et al. 2003); **Equilibrium concentration of P derived from pyromorphite solubility product

(KSP from Nriagu (1974)). Abbreviations: Cal = calcite; EQ = equilibration; prec. = precipitated.

Figure 7. log(aPb/a^2H^+)-pH-diagrams showing the stability relations of the most important secondary lead minerals as well as the predominance relations between some lead ions/complexes. Diagram (A) shows fluid evolution path in relation to different amounts pyrite reacting (including fluid paths (l), (m), (n), (o)). Diagram (B) shows the fluid evolution paths of some natural water samples from different localities from the Schwarzwald from Göb et al. (2011, 2013a, 2013b) and Markl et al. (2014a). Notice, the continuous lines are only valid for the values illustrated in the lower right corner. *Maximum P-concentration (Kaiser et al. 2003); **Equilibrium concentration of P derived from pyromorphite solubility product (logKs from Nriagu (1974)).

Figure 8: Combined reflected and transmitted light image of pyrite which is partly converted to goethite and is separated from cerussite by a zone of anglesite. Pyrite weathering is contemplated to produce H^+ during weathering subsequently stabilizing anglesite at the rims of the partly weathered pyrite rim (cf. Figure 7A). Width of photograph is about 430 µm.

Figure 9. (A) Solubility diagram of the most important secondary lead minerals anglesite, cerussite and Cl-pyromorphite in equilibrium with fluid 1.

Figure 10. Sketch of an oxidation zone, reflecting the different assumptions, leading to the growth rate equation (Eq. (6)). Abbreviations: yrs. = years.

Figure 11. (A) Calculated growth duration of a pyromorphite crust of different thicknesses with a constant dewatering area. (B) Calculated growth duration of a 1 mm thick

734 pyromorphite crust according to the dewatered area. (C) Picture of a light green pyromorphite
735 sinter growing on a wall of a former mine (photograph by J. Scovill). Abbreviations: yrs. =
736 years.

737

738 **Tables**

739

740 **Table 1.** Studied samples of weathered galena along the localities (Fig. 1), mineralization
741 type and host rocks of the respective hydrothermal veins.

No	Locality	Area	Sample numbers	Mineralization type	Host rock
1	Karlstollen mine	Badenweiler	MK-11, MK-14	Qz-Bar-Gn	Rhyolite, Shist
2	Hausbaden mine	Badenweiler	MK-12, MK-13	Qz-Bar-Fl-Gn-(Sph)-(Ccp)	Granite
3	Wilhelminenstollen mine	Badenweiler	MK-15, MK-16	Qz-Bar-Gn	Granite
4	Lisbühl-West mine	Todtnau	MK-17	Fl-Bar-Qz-Gn-Py	Gneiss
5	Todtnauer Hütte outcrop	Feldberg	GM-1901 - GM1918b	Sid/Goe-Gal	Gneiss
6	no exact location	Schauinsland	MK-19, MK-20, MK-21	Qz-Gn±Sph	Migmatite
7	Michael mine	Lahr	MK-01 - MK-10	Bar-Qz-Gn-Sph-native arsenic	Gneiss, Granite

Bar = barite, Fl = fluorite, Gn = galena, Goe = goethite, Py = pyrite Qz = Quartz, Sph = Sphalerite

742

743 **Table 2.** Input parameters for the PHREEQC/PHREEPLOT modeling

Input parameter	Values for the PHREEQC/ PHREEPLOT modeling
pH-range	pH = 2 to pH = 10
start pH value	pH= 4.9 [1], [2], [3], [5]
logCO_2 partial pressure	-0.4 bar – -3.4 bar
logO_2 partial pressure	-0.68 bar
Cl concentration	2.60×10^{-4} M [7], [8], [9], [10]
P range	Maximum: 1.00×10^{-5} M [4]
	Minimum: 3.56×10^{-10} M [*]
S concentration	1.35×10^{-4} M [6], [7], [8], [9], [10]
Pb-concentration	Set as variable

References: [1] = Mrose (1966), [2] = Verhoeven et al. (1987), [3] = Négrel and Roy (1998), [4] = Kaiser et al. (2003) [5] = Polkowska et al.

(2005), [6] = Bucher et al. (2009), [7] = Göb et al. (2011), [8] = Göb et al. (2013a) , [9] = Göb et al. (2013b), [10] = Markl et al. (2014a). [*] = Equilibrium concentration of P derived from congruent pyromorphite dissolution (logKs from Nriagu (1974)).

744

745

Figure 1

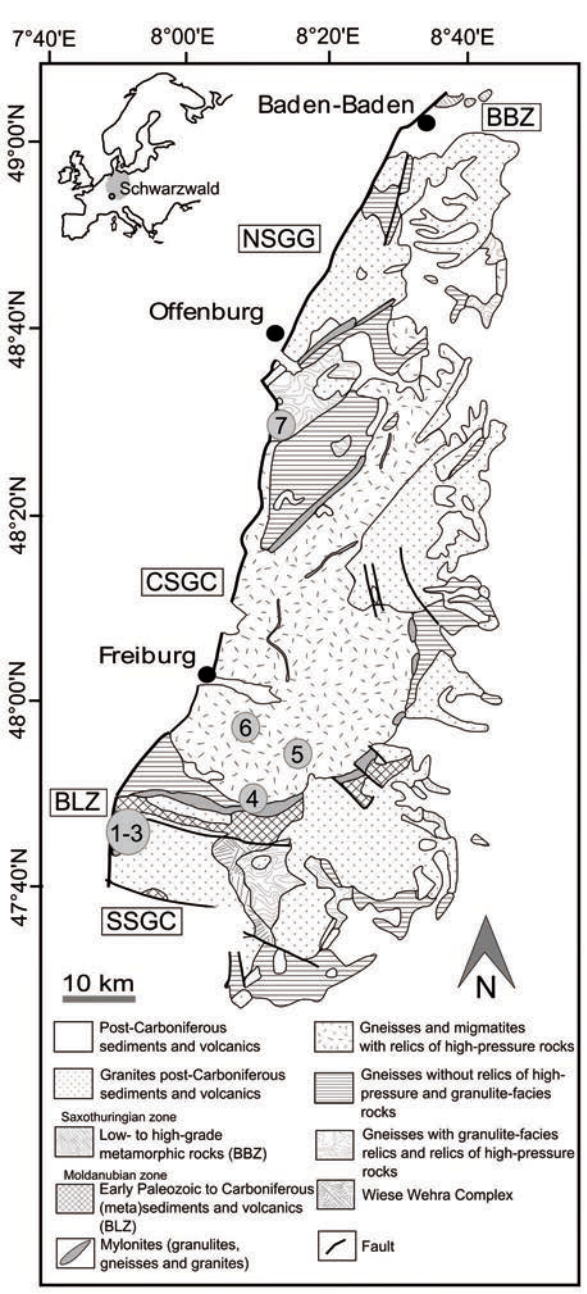
7°40'E
8°00'E
8°20'E
8°40'E
49°00'N
48°40'N
48°20'N
48°00'N
47°40'N
Schwarzwald
Baden-Baden
BBZ
NSGG
Offenburg
7
CSGC
Freiburg
6
5
4
BLZ
1-3
SSGC
10 km
N
Post-Carboniferous sediments and volcanics
Granites post-Carboniferous sediments and volcanics
Saxothuringian zone
Low- to high-grade metamorphic rocks (BBZ)
Moldanubian zone
Early Paleozoic to Carboniferous (meta)sediments and volcanics (BLZ)
Mylonites (granulites, gneisses and granites)
Gneisses and migmatites with relics of high-pressure rocks
Gneisses without relics of high-pressure and granulite-facies rocks
Gneisses with granulite-facies relics and relics of high-pressure rocks
Wiese Wehra Complex
Fault

Figure 2

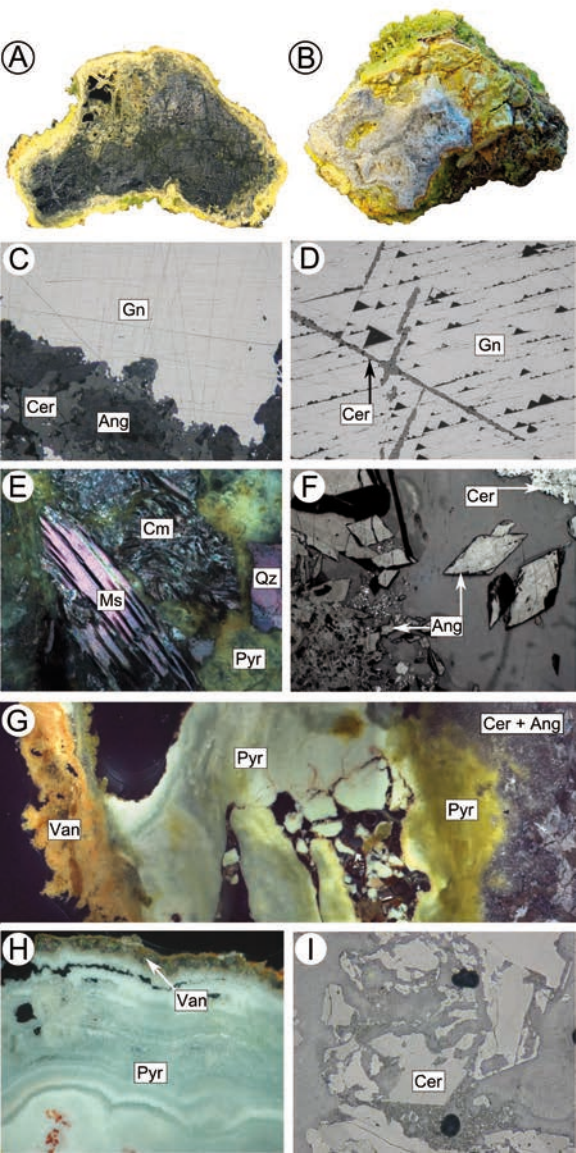
A
B
C
Gn
Cer
Ang
D
Gn
Cer
E
Cm
Ms
Qz
Pyr
F
Cer
Ang
G
Cer + Ang
Pyr
Pyr
Van
H
Van
Pyr
I
Cer

Figure 3

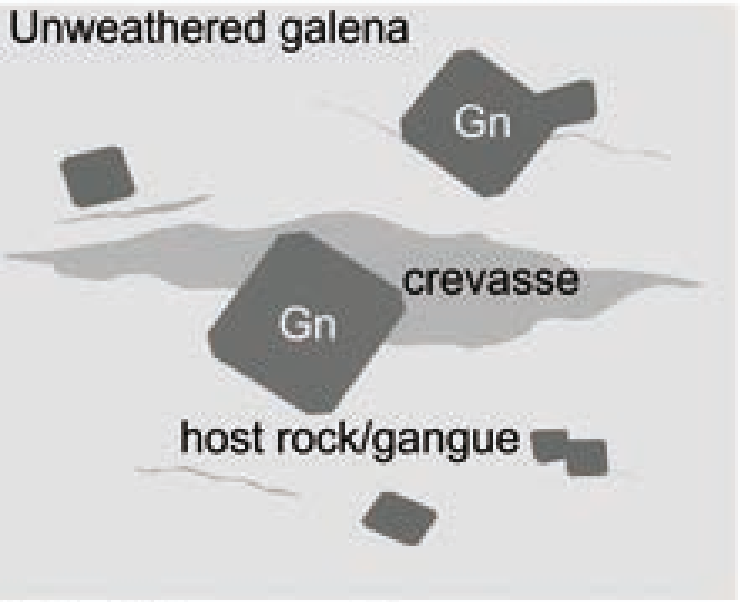
Unweathered galena
Gn
crevasse
Gn
host rock/gangue

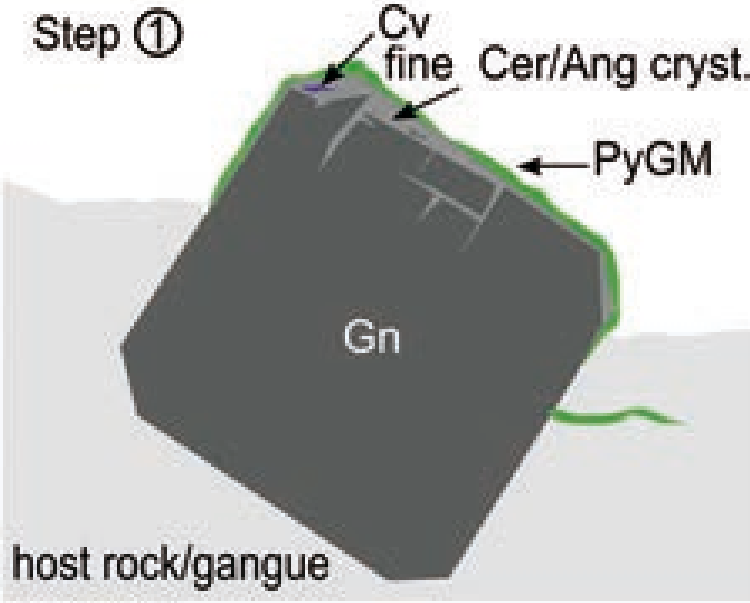
Step ①
Cv
fine Cer/Ang cryst.
PyGM
Gn
host rock/gangue

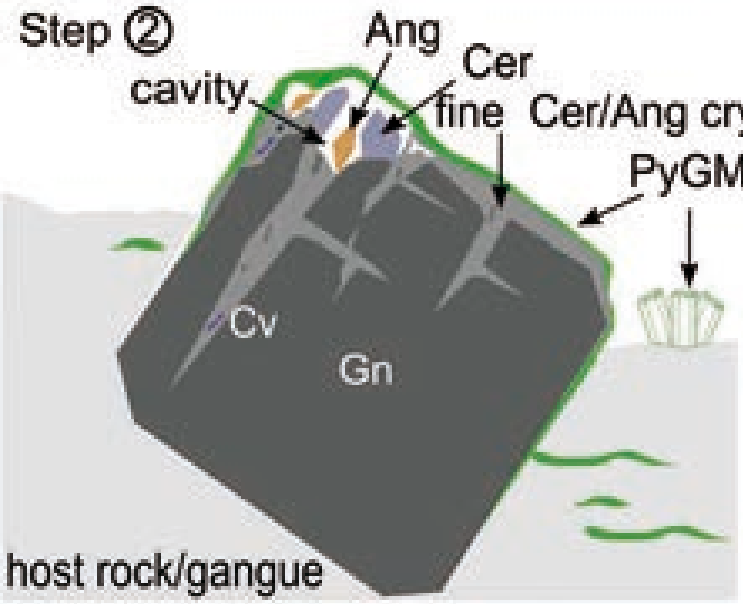
Step ②
Ang
Cer
cavity
fine Cer/Ang cryst.
PyGM
Cv
Gn
host rock/gangue

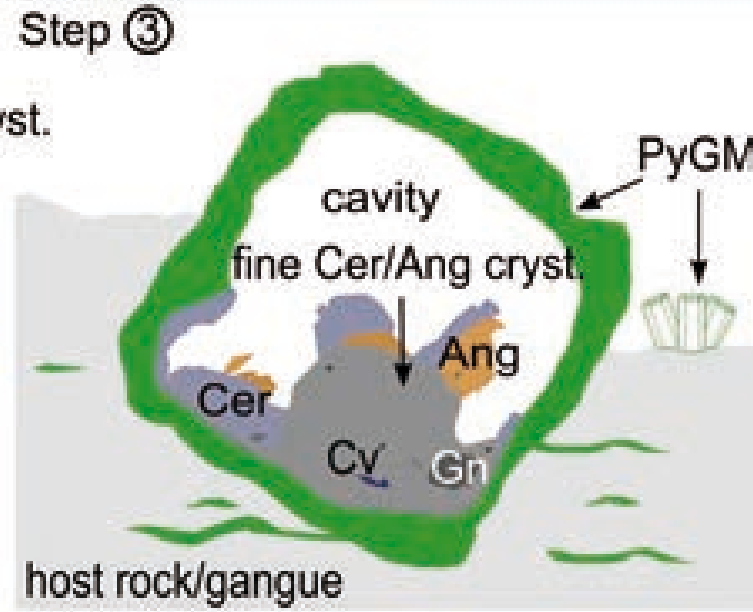
Step ③
PyGM
cavity
fine Cer/Ang cryst.
Ang
Cer
Cv
Gn
host rock/gangue

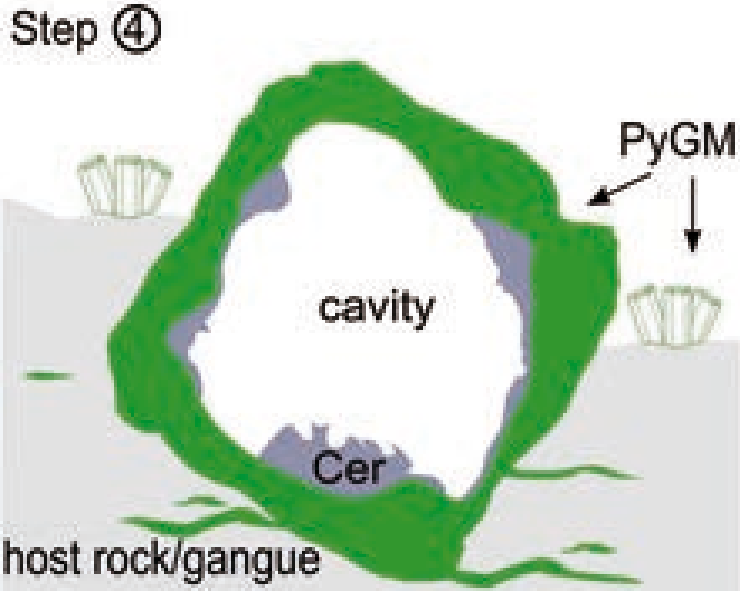
Step ④
PyGM
cavity
Cer
host rock/gangue

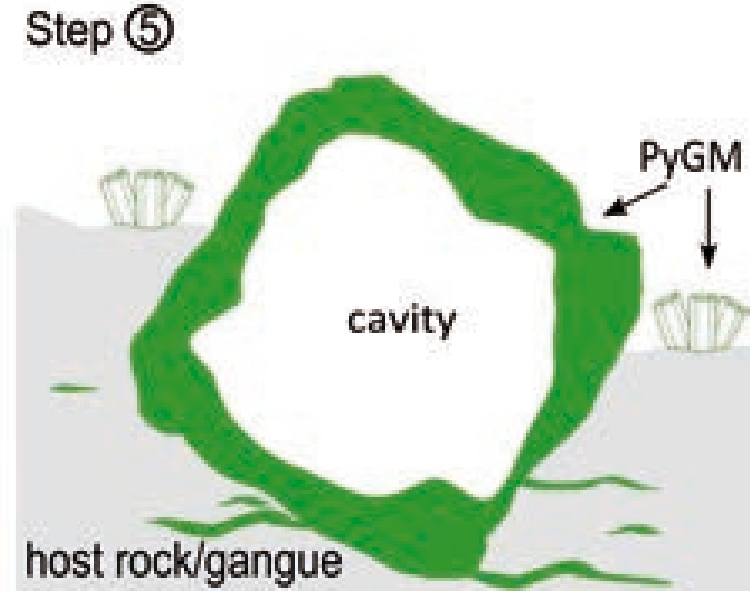
Step ⑤
PyGM
cavity
host rock/gangue

Figure 4

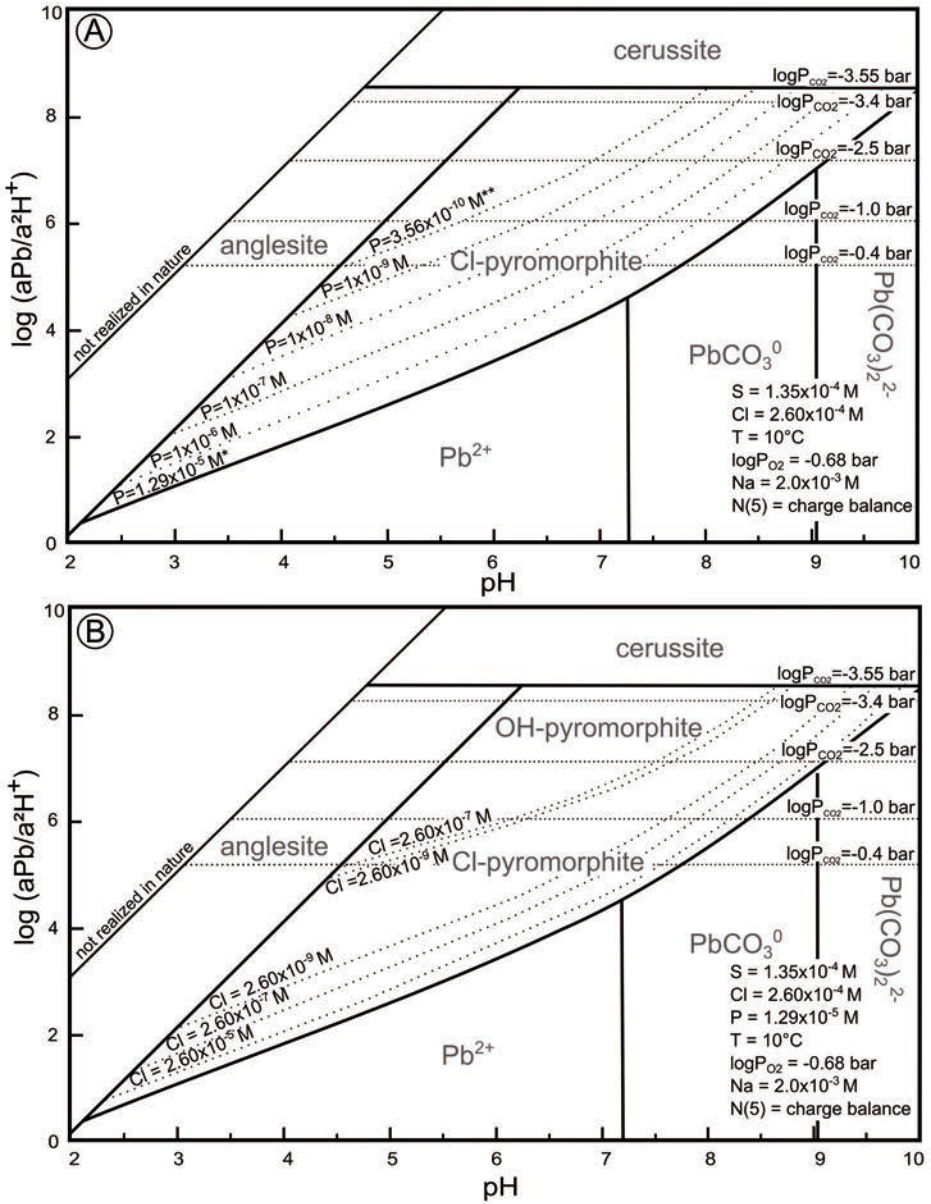
A
cerussite
logP$_{CO2}$=-3.55 bar
logP$_{CO2}$=-3.4 bar
logP$_{CO2}$=-2.5 bar
logP$_{CO2}$=-1.0 bar
logP$_{CO2}$=-0.4 bar
anglesite
Cl-pyromorphite
not realized in nature
P=3.56x10^{-10} M**
P=1x10^{-9} M
P=1x10^{-8} M
P=1x10^{-7} M
P=1x10^{-6} M
P=1.29x10^{-5} M*
Pb^{2+}
PbCO$_3^0$
Pb(CO$_3$)$_2^{2-}$
S = 1.35x10^{-4} M
Cl = 2.60x10^{-4} M
T = 10°C
logP$_{O2}$ = -0.68 bar
Na = 2.0x10^{-3} M
N(5) = charge balance
log (aPb/a^{2}H$^+$)
pH
B
cerussite
logP$_{CO2}$=-3.55 bar
logP$_{CO2}$=-3.4 bar
OH-pyromorphite
logP$_{CO2}$=-2.5 bar
logP$_{CO2}$=-1.0 bar
logP$_{CO2}$=-0.4 bar
anglesite
Cl-pyromorphite
not realized in nature
Cl =2.60x10^{-7} M
Cl =2.60x10^{-9} M
Cl = 2.60x10^{-9} M
Cl = 2.60x10^{-7} M
Cl = 2.60x10^{-5} M
Pb^{2+}
PbCO$_3^0$
Pb(CO$_3$)$_2^{2-}$
S = 1.35x10^{-4} M
Cl = 2.60x10^{-4} M
P = 1.29x10^{-5} M
T = 10°C
logP$_{O2}$ = -0.68 bar
Na = 2.0x10^{-3} M
N(5) = charge balance
log (aPb/a^{2}H$^+$)
pH

Figure 5

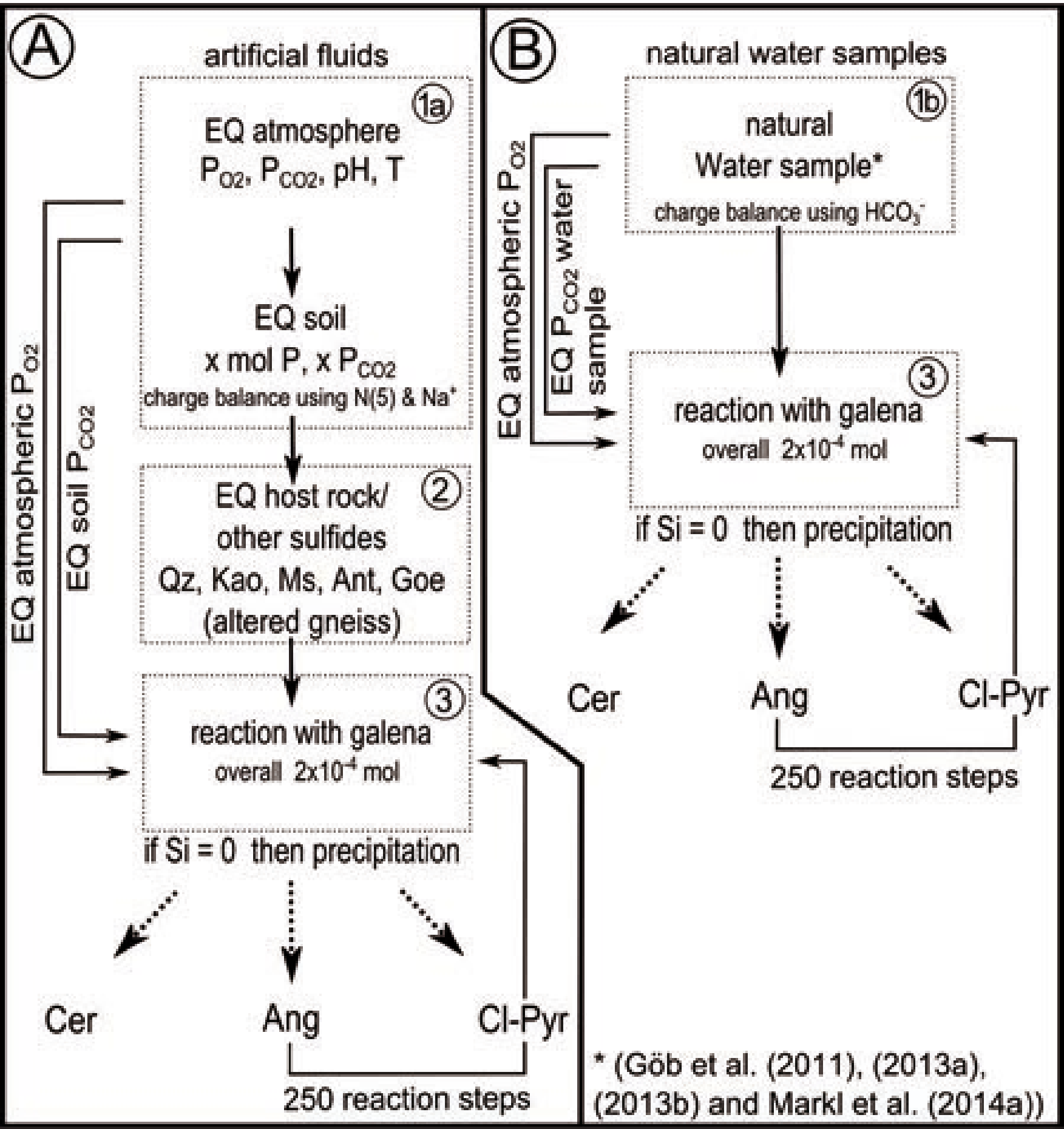
A
artificial fluids
1a
EQ atmosphere
P_{O2}, P_{CO2}, pH, T
EQ soil
x mol P, x P_{CO2}
charge balance using N(5) & Na^+
EQ host rock/
other sulfides
Qz, Kao, Ms, Ant, Goe
(altered gneiss)
2
3
reaction with galena
overall $2x10^{-4}$ mol
if Si = 0 then precipitation
Cer
Ang
Cl-Pyr
250 reaction steps
EQ atmospheric P_{O2}
EQ soil P_{CO2}
B
natural water samples
1b
natural
Water sample*
charge balance using HCO_3^-
EQ atmospheric P_{O2}
EQ P_{CO2} water sample
3
reaction with galena
overall $2x10^{-4}$ mol
if Si = 0 then precipitation
Cer
Ang
Cl-Pyr
250 reaction steps
* (Göb et al. (2011), (2013a), (2013b) and Markl et al. (2014a))

Figure 6

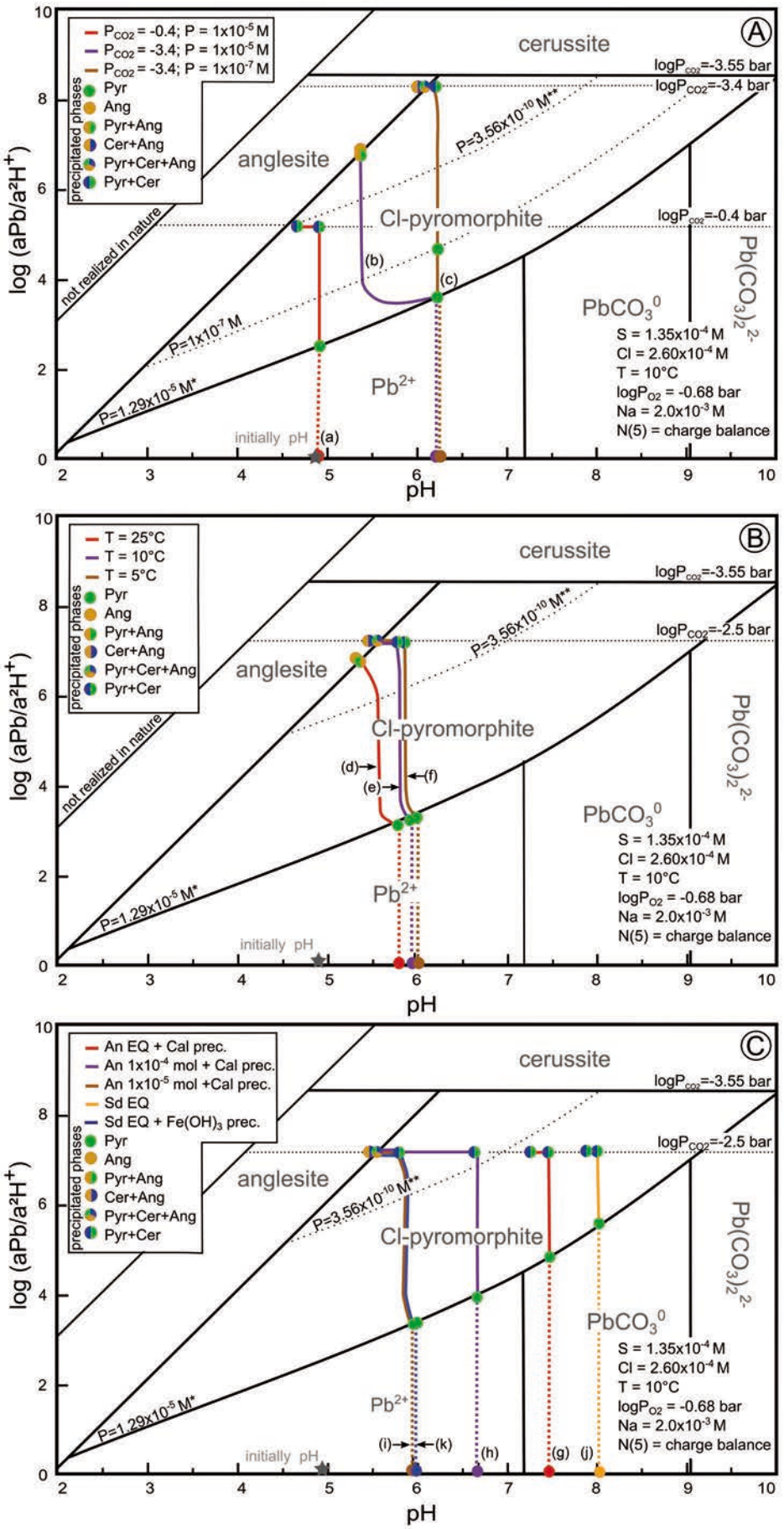
A
B
C
cerussite
anglesite
Cl-pyromorphite
not realized in nature
precipitated phases
Pyr
Ang
Pyr+Ang
Cer+Ang
Pyr+Cer+Ang
Pyr+Cer
P=3.56x10-10 M**
P=1x10-7 M
P=1.29x10-5 M*
logPCO2=-3.55 bar
logPCO2=-3.4 bar
logPCO2=-0.4 bar
logPCO2=-2.5 bar
Pb(CO3)2 2-
PbCO3 0
Pb2+
S = 1.35x10-4 M
Cl = 2.60x10-4 M
T = 10°C
logPO2 = -0.68 bar
Na = 2.0x10-3 M
N(5) = charge balance
initially pH
(a)
(b)
(c)
(d)
(e)
(f)
(g)
(h)
(i)
(j)
(k)
PCO2 = -0.4; P = 1x10-5 M
PCO2 = -3.4; P = 1x10-5 M
PCO2 = -3.4; P = 1x10-7 M
T = 25°C
T = 10°C
T = 5°C
An EQ + Cal prec.
An 1x10-4 mol + Cal prec.
An 1x10-5 mol +Cal prec.
Sd EQ
Sd EQ + Fe(OH)3 prec.
log (aPb/a2H+)
pH

Figure 7

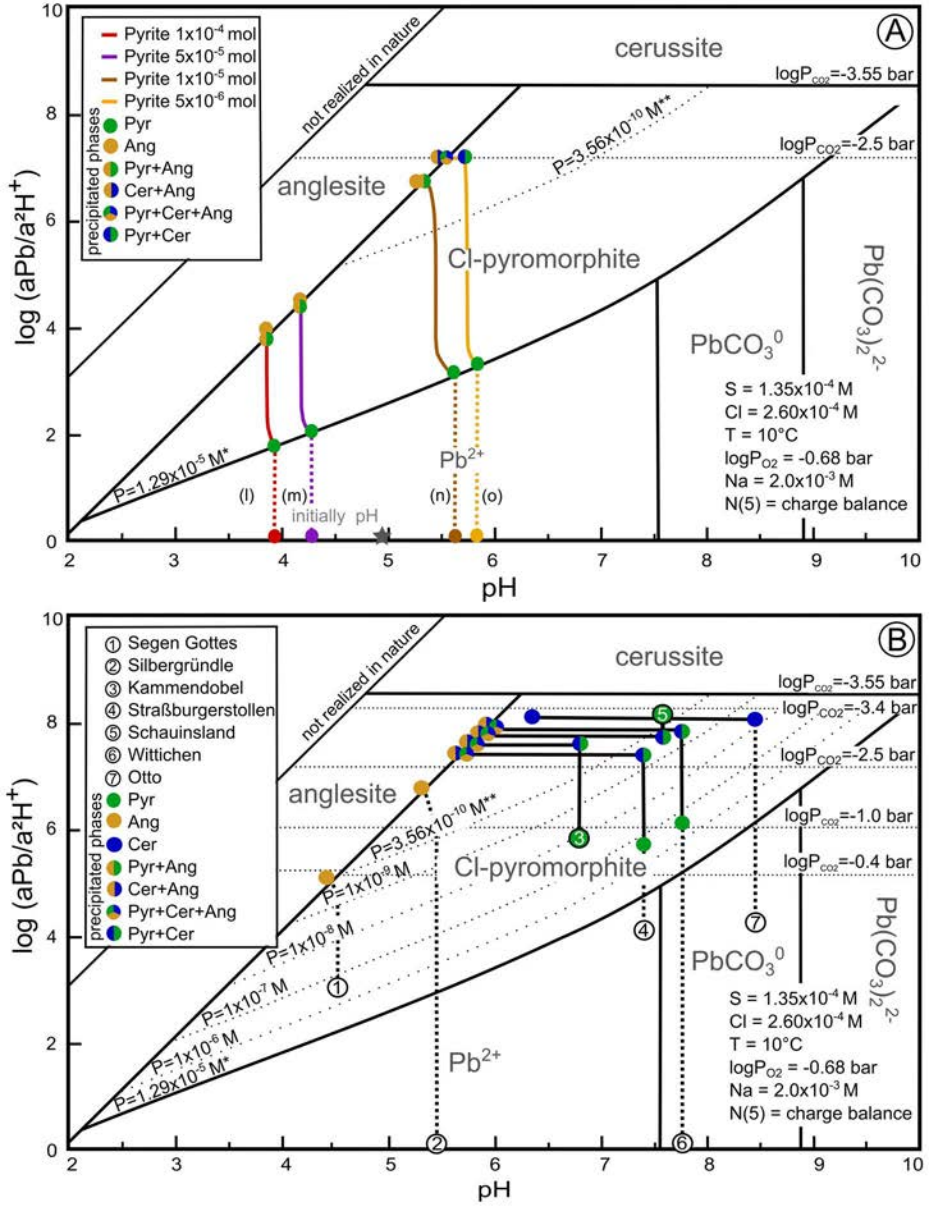
A
Pyrite 1x10-4 mol
Pyrite 5x10-5 mol
Pyrite 1x10-5 mol
Pyrite 5x10-6 mol
precipitated phases
Pyr
Ang
Pyr+Ang
Cer+Ang
Pyr+Cer+Ang
Pyr+Cer
not realized in nature
cerussite
logPCO2=-3.55 bar
logPCO2=-2.5 bar
P=3.56x10-10 M**
anglesite
Cl-pyromorphite
Pb(CO3)2 2-
PbCO3 0
S = 1.35x10-4 M
Cl = 2.60x10-4 M
T = 10°C
logPO2 = -0.68 bar
Na = 2.0x10-3 M
N(5) = charge balance
P=1.29x10-5 M*
Pb2+
(l)
(m)
(n)
(o)
initially pH
log (aPb/a2H+)
pH
B
① Segen Gottes
② Silbergründle
③ Kammendobel
④ Straßburgerstollen
⑤ Schauinsland
⑥ Wittichen
⑦ Otto
Pyr
Ang
Cer
Pyr+Ang
Cer+Ang
Pyr+Cer+Ang
Pyr+Cer
precipitated phases
not realized in nature
cerussite
logPCO2=-3.55 bar
logPCO2=-3.4 bar
logPCO2=-2.5 bar
logPCO2=-1.0 bar
logPCO2=-0.4 bar
P=3.56x10-10 M**
P=1x10-9 M
P=1x10-8 M
P=1x10-7 M
P=1x10-6 M
P=1.29x10-5 M*
anglesite
Cl-pyromorphite
Pb(CO3)2 2-
PbCO3 0
Pb2+
S = 1.35x10-4 M
Cl = 2.60x10-4 M
T = 10°C
logPO2 = -0.68 bar
Na = 2.0x10-3 M
N(5) = charge balance
log (aPb/a2H+)
pH

Figure 8

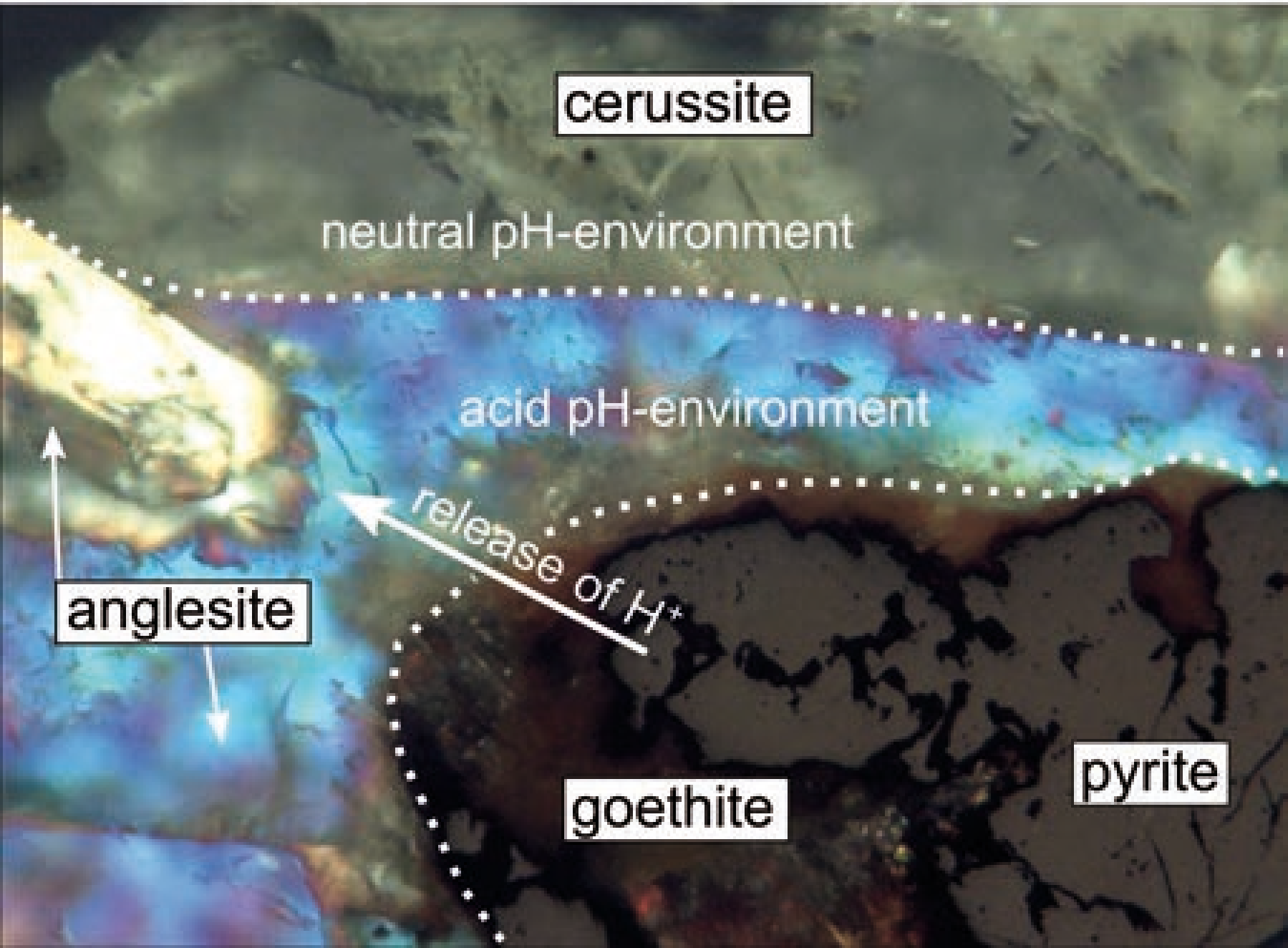
cerussite
neutral pH-environment
acid pH-environment
release of H+
anglesite
goethite
pyrite

Figure 9

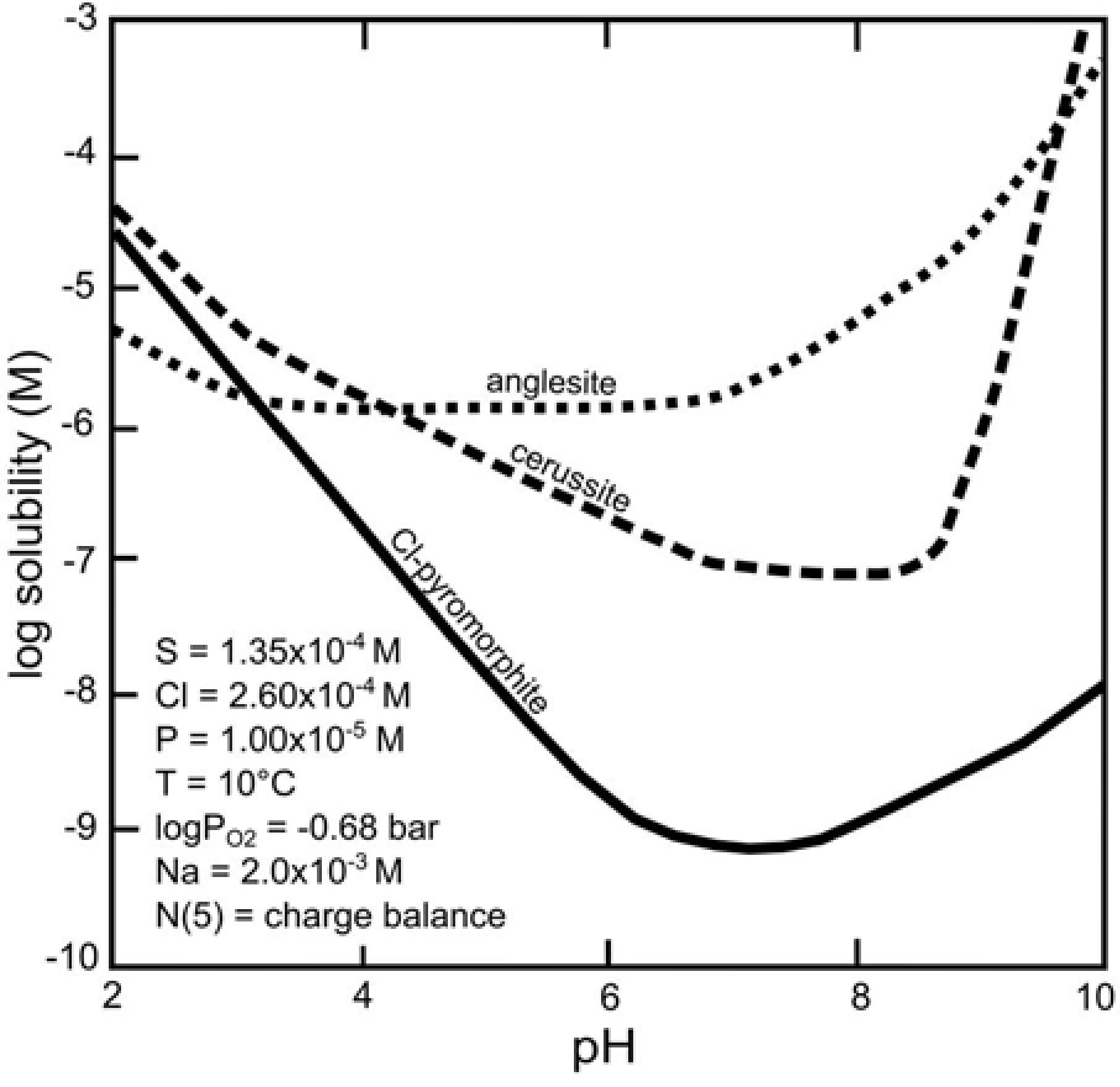
-3
-4
-5
-6
-7
-8
-9
-10
log solubility (M)
2
4
6
8
10
pH
anglesite
cerussite
Cl-pyromorphite
S = 1.35x10-4 M
Cl = 2.60x10-4 M
P = 1.00x10-5 M
T = 10°C
logPO2 = -0.68 bar
Na = 2.0x10-3 M
N(5) = charge balance

Figure 10

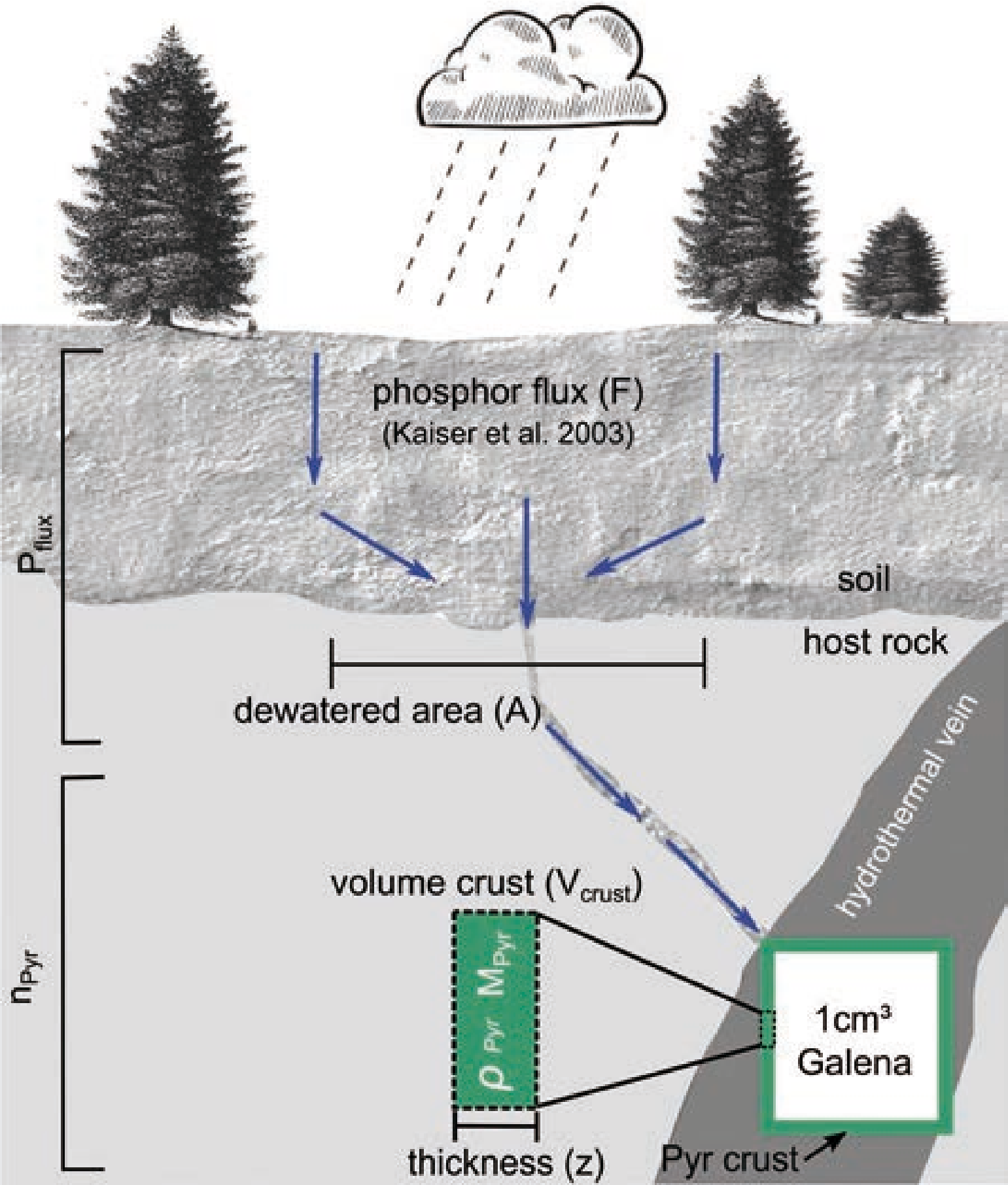
phosphor flux (F)
(Kaiser et al. 2003)
P_{flux}
soil
host rock
dewatered area (A)
hydrothermal vein
volume crust (V_{crust})
n_{Pyr}
ρ_{Pyr} M_{Pyr}
1cm³
Galena
thickness (z)
Pyr crust

Figure 11

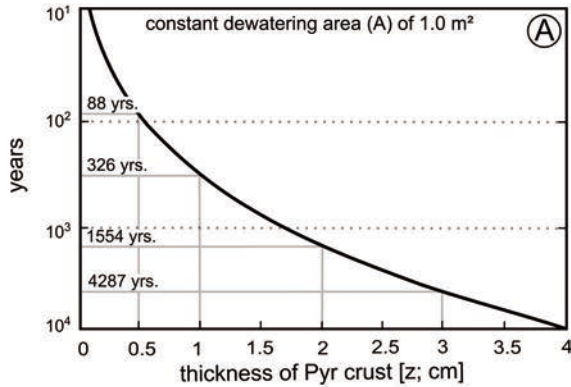
constant dewatering area (A) of 1.0 m²
A
88 yrs.
326 yrs.
1554 yrs.
4287 yrs.
years
thickness of Pyr crust [z; cm]

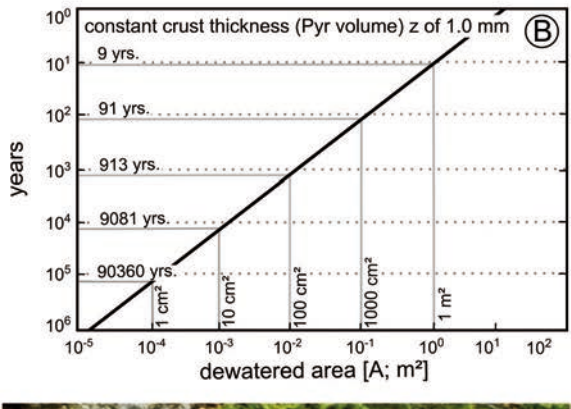
constant crust thickness (Pyr volume) z of 1.0 mm
B
9 yrs.
91 yrs.
913 yrs.
9081 yrs.
90360 yrs.
1 cm²
10 cm²
100 cm²
1000 cm²
1 m²
years
dewatered area [A; m²]

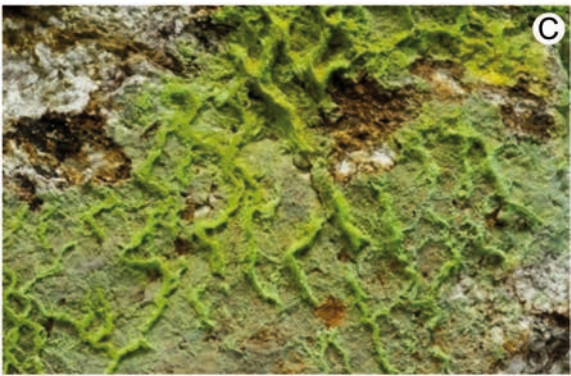
C